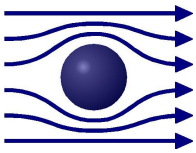

TECHNISCHE
UNIVERSITÄT
MÜNCHEN

WALTHER - MEISSNER -
INSTITUT FÜR TIEF -
TEMPERATURFORSCHUNG

BAYERISCHE
AKADEMIE DER
WISSENSCHAFTEN

Design, Fabrication and Characterization of a Microwave Resonator for Circuit QED

Diploma Thesis

Susanne Hofmann

Advisor: Prof. Dr. Rudolf Gross

Munich, 30 March 2007

TECHNISCHE UNIVERSITÄT MÜNCHEN

Contents

1 Motivation and Outline

Quantum Information Processing is a field with a huge variety of aims, purposes and applications. It includes, among others, the large field of quantum *computing*, a subject of interest in many research areas.

There are some realizations even with superconducting devices (e.g. the charge qubit) or, to stay in the field of solid state physics, quantum dots, realized with semiconductors and also in the field of atomic physics where individual atoms play the role of quantum two-level systems. In liquid nuclear magnetic resonance (NMR) the factorization of 15 was realized with seven spin-1/2 nuclei in a molecule used as quantum bits [20]. The calculation was done with the Shor algorithm which is well known in quantum information theory [17]. Beyond the experiments done at different institutes also companies are interested in the field of building a quantum computer. Recently D-Wave Systems, Inc., Canada presented their proposal of a quantum computer in public [1].

Although many different qubits have been realized, one central problem in quantum computing is the coupling of qubits, in order to make operations and generate entangled quantum states. The multidisciplinary field of quantum computing yielded a simple scheme. In quantum optics quantum computing is realized with atoms placed in a 3d cavity, which has the advantage of providing a readout scheme for the qubit. Using cavities with wavelengths in the millimeter regime it is possible to copy this scheme directly to the world of solid state qubits. This idea was realized with quantum dots [15] and proposed for superconducting charge qubits by Blais et al. [2]. In this work the regimes of zero and large detuning between the artificial atom and the cavity were discussed. In the large detuning regime the lifetime of a qubit will be enhanced and a dispersive quantum non-demolition readout of the qubit will be possible. Also control and entanglement of qubits by using the cavity modes as a "bus" system is possible. The resonator with a charge qubit inside was realized by Frunzio et al. [6], Wallraff et al. [21] experimentally verified the strong coupling of a qubit and a cavity in the resonant and the detuned regime for the first time. The Rabi splitting of the interaction of the cavity and the qubit was observed. Yang et al. [23] investigated the implementation of entanglement of two Cooper pair boxes within a microwave cavity in detail. They found that the information transfer from one qubit to another can be realized with high fidelity. The cavity has the advantage of working like a magnetic filter, therefore, decoherence caused by the external environment is strongly suppressed. With frequency matching it is possible to selectively couple microwave pulses and any particular qubit in the cavity.

While these experiments deal with charge qubits a new approach will be done with flux qubits. This work is a small step into this new field of flux qubits in a cavity. Our aim is to produce and understand high Q cavities. Later on these will be used for placing a flux qubit inside, in order to compare this type of realization with the one with a charge qubit and to analyze decoherence and noise effects (e.g. charge noise). A single qubit will be placed in

the antinode of the magnetic field of the resonator operating at the first mode of resonance. By using higher modes and placing more qubits in the different antinodes one can couple those qubits. Coupling of more qubits with a two dimensional square lattice of resonators was proposed recently [10].

As mentioned above this work deals with cavities for superconducting flux qubits. These cavities are realized by superconducting coplanar waveguide resonators. Therefore, the **second chapter** is dedicated to the theoretical issues concerning the coplanar waveguide, general issues of the resonator and the influence of superconductivity on both. At the end, a small overview of the method of scattering parameters measured in this work is given. The **third chapter** gives a brief overview of the design process of the resonators. The fabrication is outlined in the **fourth chapter**. The **fifth chapter** presents S-parameter measurements for three different designs, different resonance frequencies, different coupling and two substrate materials. At the end of this chapter the results are summarized and compared to theoretical predictions. Simulations done in order to predict the measured results theoretically, at the Walther-Meißner-Institut and in collaboration with the institute of nanoelectronics are shown in the **sixth chapter**. Last a conclusion and outlook is given.

2 Theoretical Description of a CPW Resonator

The aim of this thesis is to design a resonator for frequencies in the GHz-regime fabricated in coplanar waveguide (CPW) technique. This chapter deals first with the theory of CPWs based on the conformal mapping method [16]. The calculation of the characteristic impedance, capacitance and inductance of a CPW is discussed in detail. Then we briefly present how the use of different substrate materials influences the characteristics of the CPW. At the end of the first section, the dispersion and attenuation aspects are given.

After this, effects of using a superconducting material (in our case Niobium) on the impedance and attenuation are introduced.

The third part of this chapter discusses some basic details of resonators, especially resonance frequency, quality factor and coupling to the environment. The special cases of microwave and superconducting resonators are presented. The attenuation considered in the first section is extended to superconductivity and the temperature dependence of resonance frequency and quality factor of the superconducting CPW (SCCPW) is discussed.

The last section explains briefly the theory of scattering parameters used in our measurements.

2.1 The Coplanar Transmission Line

The CPW proposed by C. P. Wen in 1969 [22] was chosen for this thesis for its easy fabrication compared to other types of transmission lines. The conducting layer is directly fabricated on top of a substrate without the need for wraparounds or via holes. This means, only a single layer technology is required, therefore, the CPW can be fabricated in-house at the Walther-Meißner-Institut. Another advantage is the very small radiation loss which would influence the quality factor of the resonator. Furthermore, the characteristic impedance is directly related to the ratio of the width of the inner strip to the width of the gap, so it was possible to design various geometries easily. In this thesis three different designs were realized. Taking superconductivity into account, with the so called kinetic inductance, one can see from Figure 2.8 in subsection 2.2.1 that the CPW is not very sensitive to the kinetic inductance.

This section deals with two classifications of CPWs, shown in Figure 2.1. The used equations and further information can be found in reference [18]. A conventional CPW on a dielectric substrate consists of a center strip conductor with semi-infinite ground planes on either side. However, in a real circuit the ground planes are large but of finite extend. The conductor backed CPW (CBCPW) has an additional ground plane at the bottom surface of the substrate, realized by sputtering Niobium on both sides of the substrate.

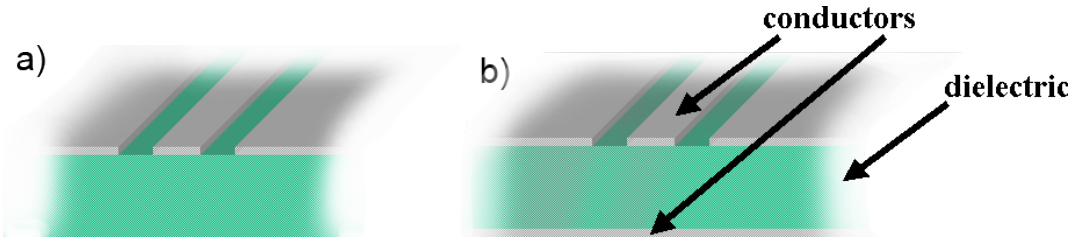

Figure 2.1: Different realizations of CPW: (a) the conventional CPW, (b) the conductor backed CPW.

The cross-sectional view of a CPW is shown in Figure 2.2. In this CPW structure a center conductor and two ground planes are superimposed on a single substrate. A brief discussion of two layer substrates, like those used in this thesis, can be found in subsection 2.1.4. We denote the CPW *center strip conductor width* by S, the *slot width* by W. The *height of the dielectric substrate* is H with a corresponding *relative permittivity* ε_r.

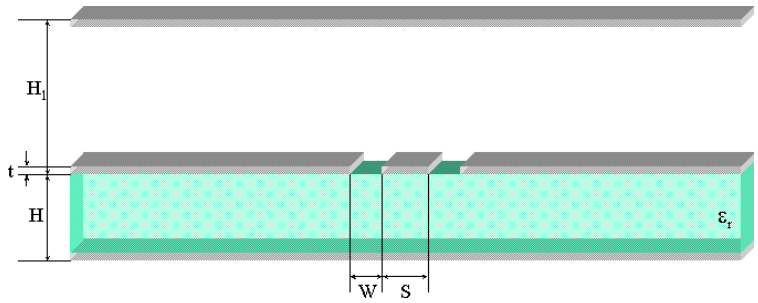

Figure 2.2: Structure of a CPW, a conducting strip and two ground planes are placed on a substrate. The CPW is shielded on top and bottom by conducting layer.

Two metal shields are placed above the CPW conductors and on the bottom surface of the dielectric substrate. H_1 denotes the height of the upper metal cover. The shielding is realized by the conducting inner side of the measurement-box. The side box walls can be neglected due to the large distance to the inner conductor. From the geometry, an *effective dielectric constant*

$$\varepsilon_{eff} = \frac{C_{CPW}}{C_{Air}} = \frac{C_{Air} + C_{diel}}{C_{Air}} = 1 + \frac{C_{diel}}{C_{Air}} \tag{2.1}$$

can be calculated as the ratio of the *capacitance of the CPW* C_{CPW} to the *capacitance of the air-filled region* C_{Air} where the total capacitance of the CPW is a sum of a *dielectric capacitance* C_{diel} and C_{Air}.

2.1.1 Constitution of Air-Filled Regions

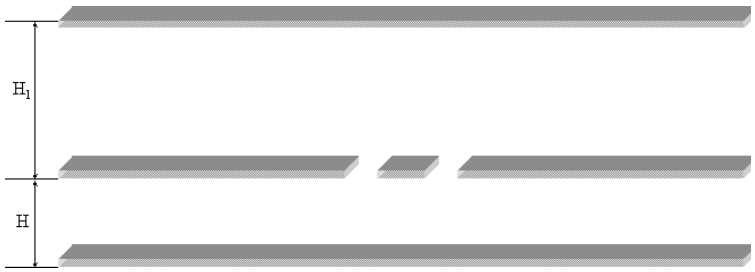

Figure 2.3: Configuration of the air capacitance of a CPW.

The partial capacitance of the CPW in the absence of all dielectric layers

$$C_{Air} = 2\varepsilon_0 \frac{K(k)}{K(k')} + 2\varepsilon_0 \frac{K(k_1)}{K(k_1')}$$

consists of the sum of the upper and the lower regions, with heights H and H_1, as shown in Figure 2.3.

$K(k)$ and $K(k')$ are the complete elliptic integrals with the moduli

$$\begin{aligned} k &= \frac{\tanh(\frac{\pi \cdot S}{4 \cdot H})}{\tanh(\frac{\pi \cdot (S+2 \cdot W)}{4 \cdot H})}, \\ k' &= \sqrt{1-k^2}, \\ k_1 &= \frac{\tanh(\frac{\pi \cdot S}{4 \cdot H_1})}{\tanh(\frac{\pi \cdot (S+2 \cdot W)}{4 \cdot H_1})}. \end{aligned} \tag{2.2}$$

.

We reduce these formula to

$$k \approx \frac{\frac{\pi \cdot S}{4 \cdot H}}{\frac{\pi \cdot (S+2 \cdot W)}{4 \cdot H}} = \frac{S}{S+2 \cdot W} \tag{2.3}$$

in the case of large heights H and H_1.

The capacitance of the air-filled regions simplifies to:

$$C_{Air} = 4\varepsilon_0 \frac{K(k)}{K(k')}$$

2.1.2 Constitution of Dielectric Filled Regions

2.1.2.1 CPW

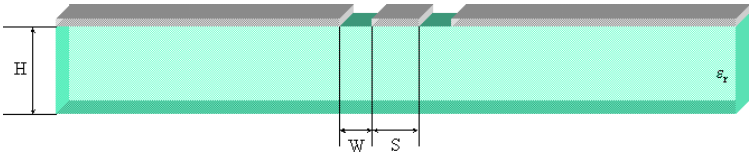

Figure 2.4: Configuration of the dielectric capacitance of a CPW.

The capacitance in the dielectric region

$$C_{diel} = 2\varepsilon_0(\varepsilon_r - 1)\frac{K(k_{diel})}{K(k'_{diel})} \tag{2.4}$$

is calculated in analogy to C_{air}, with the modulus

$$k_{diel} = \frac{\sinh(\frac{\pi \cdot S}{4 \cdot H})}{\sinh(\frac{\pi \cdot (S+2 \cdot W)}{4 \cdot H})}. \tag{2.5}$$

Since there is no dielectric other than air in the upper region ε_r is set equal to 1 in (2.4) and $C_{diel,top}$ becomes zero.

The parenthesized term $(\varepsilon_r - 1)$ can be interpreted as a substitution of air (ε_r = 1, used for C_{Air}) with the dielectric substrate.

It is worth mentioning here that for C_{Air} one uses tanh in the modulus and sinh for the dielectric region.

The calculation can be structured by defining a *filling factor q* giving

$$\varepsilon_{eff} = 1 + q(\varepsilon_r - 1). \tag{2.6}$$

In the case of Figure 2.2

$$q = \frac{\frac{K(k_{diel})}{K(k'_{diel})}}{\frac{K(k)}{K(k')} + \frac{K(k_1)}{K(k'_1)}}, \tag{2.7}$$

which tends to $\frac{1}{2}$ for very large heights.

2.1.2.2 CBCPW

The difference of a conductor backed to a conventional CPW is the existence of a ground plane on the bottom of the dielectric layer, realized with the same conductor material the CPW is made of. In case of a CBCPW the dielectric region is treated differently. One uses a different

$$k_{diel} = \frac{\tanh(\frac{\pi \cdot S}{4 \cdot H})}{\tanh(\frac{\pi \cdot (S+2 \cdot W)}{4 \cdot H})} = k$$

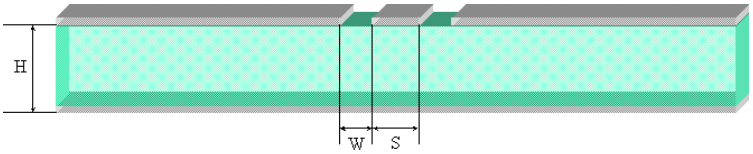

Figure 2.5: Configuration of the dielectric capacitance of a CBCPW.

for the calculation of C_{CPW} (2.4).

That means, the moduli of the dielectric and the air-filled regions are equal. The parameter q simplifies to

$$q = \frac{\frac{K(k)}{K(k')}}{\frac{K(k)}{K(k')} + \frac{K(k_1)}{K(k_1')}}, \tag{2.8}$$

which tends to $\frac{1}{2}$ for very large heights again.

2.1.2.3 Isotropy of the Dielectric

The relative permittivity ε_r (used in (2.4)) and the height of the substrate H (see e.g. (2.5)) depend on the isotropy of the dielectric material.

In this work Silicon and Sapphire are used as substrate materials.

Silicon is an isotropic material with $\varepsilon_r = 11.9$.

For *Sapphire* one needs to replace the relative permittivity with an effective permittivity

$$\varepsilon_r = \sqrt{\varepsilon_{x,z} \cdot \varepsilon_y} = 10.34$$

with $\varepsilon_y = 11.5$ (c-axis) and $\varepsilon_{x,z} = 9.3$ (a,b-axis) according to [3].

The height has to be replaced by

$$H_e = \sqrt{\frac{\varepsilon_{x,z}}{\varepsilon_y}} \cdot H = 0.9H$$

2.1.3 Summary of Capacitance Calculations

Using C_{Air} and C_{diel}, as defined in the last subsections, the *phase velocity* v_{ph} and the *wave impedance* Z_c can be calculated:

$$v_{ph} = \frac{c_0}{\sqrt{\varepsilon_{eff}}} \tag{2.9}$$

$$\begin{aligned} Z_c &= \frac{1}{C_{CPW} v_{ph}} = \frac{\sqrt{\varepsilon_{eff}}}{c_0 C_{CPW}} \\ &= \frac{Z_0}{2 \cdot \sqrt{\varepsilon_{eff}} \cdot \left(\frac{K(k)}{K(k')} + \frac{K(k_1)}{K(k_1')} \right)} \end{aligned} \tag{2.10}$$

Calculations show that the upper shielding of the CPW can be neglected for $H_1 \geq 1$ mm. At a box height of 1 mm, the difference between the exact value of Z_c with (2.2) and the approximations for large heights (2.3) is $\Delta Z_{CS} = 8.4 \cdot 10^{-4}\ \Omega$ which results in a ratio $\frac{\Delta Z_{CS}}{Z_{CS}}$ of $1.6 \cdot 10^{-5}$.

In our design, the cover of the box is 2 mm above the CPW conductor. Hence, we can assume $k_1 = \frac{S}{S+2 \cdot W}$.

From (2.9) or (2.10) and (2.1) the *inductance* L_{CPW} can be calculated as follows:

$$\begin{aligned} C_{CPW} &= \varepsilon_{eff} \cdot C_{Air} \\ &= 2 \cdot \varepsilon_0 \cdot \varepsilon_{eff} \cdot \left(\frac{K(k_1)}{K(k_1')} + \frac{K(k)}{K(k')} \right) \qquad (2.11) \\ \text{with} \quad v_{ph} &= \frac{1}{\sqrt{C_{CPW} \cdot L_{CPW}}} \qquad (2.12) \\ \text{or} \quad Z_{cs} &= \sqrt{\frac{L_{CPW}}{C_{CPW}}} \\ \Rightarrow L_{CPW} &= \frac{\varepsilon_0 \mu_0}{C_{Air}} \\ &= \frac{\frac{\mu_0}{2}}{\frac{K(k)}{K(k')} + \frac{K(k_1)}{(k_1')}} \qquad (2.13) \end{aligned}$$

2.1.4 Treatment of Double Layer Substrates

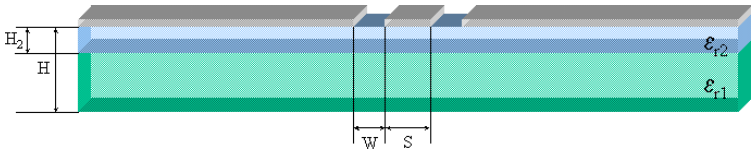

Figure 2.6: Schematic of a CPW on a double-layer dielectric substrate.

On top of the Silicon substrate which is used in this thesis, 50 nm Silicon are thermally oxidized. In Figure 2.6 a conventional CPW on a double layer substrate is shown. The two dielectric substrate thicknesses are designated $H - H_2$ and H_2 with relative permittivities ε_{r1} and ε_{r2}.

The dielectric capacitance of the dielectric region

$$C_{diel} = 2\varepsilon_0(\varepsilon_{2r} - \varepsilon_{1r}) \frac{K(k_{2diel})}{K(k_{2diel}')}$$

now is the sum of C_{diel} for a single layer substrate (2.4) for the lower dielectric and a capacitance analogous to (2.4) for the upper dielectric.

k_{2diel} is the modulus equal to the modulus of a CPW with a single layer substrate (2.5) substituting h by h_2.

One can calculate the effective permittivity

$$\varepsilon_{eff} = 1 + q_1(\varepsilon_{r1} - 1) + q_2(\varepsilon_{r2} - \varepsilon_{r1})$$

with

$$\begin{aligned} q_1 &= \frac{1}{2}\frac{K(k_{1diel})}{K(k'_{1diel})}\left[\frac{K(k)}{K(k')} + \frac{K(k_1)}{K(k'_1)}\right]^{-1}, \\ q_2 &= \frac{1}{2}\frac{K(k_{2diel})}{K(k'_{2diel})}\left[\frac{K(k)}{K(k')} + \frac{K(k_1)}{K(k'_1)}\right]^{-1}. \end{aligned}$$

The impedance here is equal to the one of a single layer substrate given by (2.10).

It can be shown that the second dielectric layer of SiO_2 with $\varepsilon_{r2} = 4.7$ influences the impedance for values of H_2 larger than 1.7 μm [12].

2.1.5 Dispersion

With the help of the spectral domain method an empirical formula to compute ε_{eff} of a CPW is obtained in reference [18].

$$\sqrt{\varepsilon_{eff}(f)} = \sqrt{\varepsilon_{eff}} + \frac{(\sqrt{\varepsilon_r} - \sqrt{\varepsilon_{eff}})}{1 + aF^{-1.8}} \tag{2.14}$$

where

$F = f/f_{TE}$ is the normalized frequency

with $f_{TE} = c_0/(4H\sqrt{\varepsilon_r - 1})$, the cutoff frequency for the lowest-order TE mode,

ε_{eff} is the effective permittivity at the quasi-static limit.

The parameter

$$\log(a) \approx u \log\left(\frac{S}{W}\right) + v$$

is calculated with

$$\begin{aligned} u &\approx 0.54 - 0.64q + 0.015q^2, \\ v &\approx 0.43 - 0.86q + 0.540q^2, \\ q &= \log\frac{S}{H}. \end{aligned}$$

With an accuracy of 5 %, the formula is valid into the THz regime in the ranges given in Table 2.1.

Calculations show that for our designs, explained in detail in chapter 3, all ranges, except for the ratio of the inner strip to height of the substrate, are in the application range. Since no better formula for the designs with parameters which are out of range could be found, (2.14) was applied to these designs, too. The cutoff frequency f_{TE} for Sapphire as substrate material is 45.4 GHz, for Silicon as substrate material we evaluate 54.4 GHz.

Figure 2.7 shows the effective dielectric constant for Silicon and Sapphire as substrate materials. We see that dispersion is negligible in the measurement range.

parameter range		$\frac{S}{W}$	$\frac{S}{H}$	ε_r	$\frac{f}{f_{TE}}$
	min	0.1	0.1	1.5	0
	max	5	5	50	10

Table 2.1: Values where (2.14) is valid.

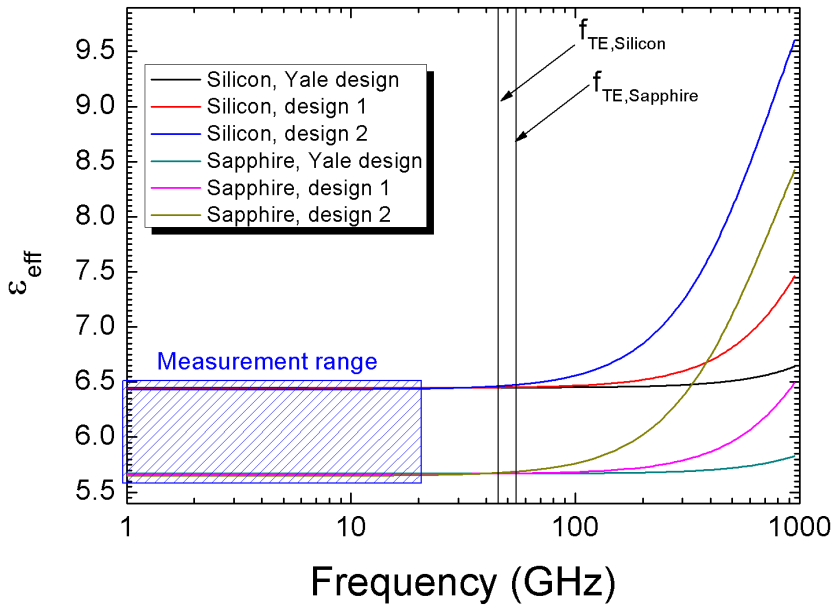

Figure 2.7: Frequency dependent effective dielectric constant ε_{eff} for all designs realized in this thesis. The cut-off frequencies are indicated by vertical lines for each substrate material.

2.1.6 Attenuation

In general the electric field $\vec{E}$ of a wave traveling along a transmission line can be written as

$$\vec{E} = \vec{E}_0 e^{(\omega t - (\alpha + i\beta)z)}$$

where z is the direction of propagation. ω is the angular frequency of the wave. We see that the wave travels with the *phase constant* β corresponding to the wavelength (imaginary part) and that it decays with distance with the *attenuation constant* α (real part).

The attenuation of a circuit should be as low as possible to avoid damping effects. Several loss sources contribute to the attenuation of a CPW per unit length:

$$\alpha = \alpha_d + \alpha_c + \alpha_r + \alpha_s \tag{2.15}$$

α_d represents the *losses in the dielectric substrate*. α_c denotes the *losses in the conductor*

(center strip and ground planes). α_r and α_s, the *radiation* and *scattering losses* can be neglected in the frequency regimes of interest according to reference [14].

2.1.6.1 Dielectric losses

The first term in (2.15) is given by [18]

$$\alpha_d = \frac{\omega}{2c_0}\frac{\varepsilon_r}{\sqrt{\varepsilon_{eff}}} q \tan\delta_e, \tag{2.16}$$

where ε_r is the relative permittivity of the substrate, $\tan\delta_e$ is the dielectric loss tangent, ε_{eff} is the effective dielectric constant defined in (2.1) and q is the filling factor defined in (2.6) and calculated as (2.7) or (2.8) for CPW or CBCPW. Table 2.2 gives values derived for the two substrate materials Silicon and Sapphire. No value for Silicon at 4K was found in literature.

substrate material	ε_r	loss tangent $\tan\delta$	attenuation α_d
Silicon	11.9	0.004 @ 10 GHz, RT [13]	0.589
Sapphire	10.34	$\approx 10^{-5}$ @ 10 GHz, RT	$1.4 \cdot 10^{-3}$
		$\approx 10^{-11}$ @ 10 GHz, 4 K (both [9])	$1.36 \cdot 10^{-8}$

Table 2.2: Dielectric loss of Silicon and Sapphire, losses are valid for all designs.

2.1.6.2 Conductor losses

The attenuation constant α_c due to conductor loss is given by [18]

$$\alpha_c = \frac{R_{sm}}{8Z_c K^2(k) S(1-k^2)} \left\{ \ln\left(\frac{S}{\Delta}\frac{(1-k)}{(1+k)}\right) + k\ln\left(\frac{S}{k\Delta}\frac{(1-k)}{(1+k)}\right)\right\}, \tag{2.17}$$

where K is the elliptic integral, its modulus is k from (2.3) introduced in subsection 2.1.1, Z_c is the impedance (2.10), the so called *stopping distance* Δ depends on the edge profile and t is the conductor thickness (drawn in Figure 2.2 on page 4).

According to [18] the attenuation is normally derived with the modified matched asymptotic expansion technique which integrates an approximate current density on the CPW conductors. When integrating over the contour integral of the current density, one could face the problem of singular fields at sharp edges. This is avoided by taking the limits of the integral at some distance (the stopping distance) just before the edge.

We can calculate the modified surface resistance

$$R_{sm} = \omega\mu_0 t \Im\left(\frac{\cot k_c t + \csc k_c t}{k_c t}\right) \tag{2.18}$$

with the complex wavenumber.

$$k_c^2 = \omega^2\mu_0\varepsilon = \omega^2\mu_0(\varepsilon_0 - i\frac{\sigma}{\omega})$$

at a frequency ω.

Which, with the help of the skin depth

$$\delta = \sqrt{\frac{2}{\omega \mu \sigma}} \tag{2.19}$$

and assuming a good conductor with $\frac{\sigma}{\omega \varepsilon_0} \gg 1$ can be written as

$$k_c^2 = -2j \left(\frac{1}{\delta} \right)^2 . \tag{2.20}$$

For example, the skin depth for copper is 0.66 μm at 10 GHz. No specific values for the attenuation are given here, due to the fact that we use superconducting CPW. Calculations including superconductivity can be found in subsection 2.2.2.

2.2 Including Superconductivity in the CPW

2.2.1 The Kinetic Inductance

For the superconducting case the CPW calculations are extended with an intuitive model. The total series inductance per unit length

$$L_{tot} = L_{kin} + L_{CPW} \tag{2.21}$$

is modeled by two parts, the external inductance per unit length L_{ext} as derived in (2.13) which accounts for magnetic energy storage not within the conductor and the internal inductance which accounts for magnetic energy storage within the conductor. The internal inductance is also called kinetic inductance L_{kin} because it originates from the inertia of the Cooper pairs. The equation for the kinetic inductance per unit length

$$L_{kin} = \mu_0 \lambda_L(T) \frac{C}{4ADK(k)} \left\{ \frac{1.7}{\sinh\left(\frac{t}{2\lambda_L(T)}\right)} + \frac{0.4}{\sqrt{\left[\left(\frac{B}{A}\right)^2 - 1\right]\left[1 - \left(\frac{B}{D}\right)^2\right]}} \right\} \tag{2.22}$$

was derived using the conformal mapping technique by Valenzuela in his Ph.D. thesis [19], with the elliptic integral K and its modulus k from equation (2.3).

The parameters A through D are given by,

$$\begin{aligned} A &= -\frac{t}{\pi} + \frac{1}{2} \cdot \sqrt{\left(\frac{2t}{\pi}\right)^2 + S^2} \\ B &= \frac{S^2}{4A} \\ C &= B - \frac{t}{\pi} + \sqrt{\left(\frac{t}{\pi}\right)^2 + W^2} \\ D &= \frac{2t}{\pi} + C \end{aligned}$$

In the expression (2.22) for L_{kin} the values 1.7 and 0.4 were obtained using partial wave synthesis [7].

The London penetration depth

$$\lambda_L(T) = \frac{\lambda_L(0)}{\left(1 - \left(\frac{T}{T_c}\right)^4\right)^{1/2}} \tag{2.23}$$

depends on temperature.

From the formula for the total inductance one can once again derive equations for the group velocity and the impedance of the CPW like in (2.12) and (2.10):

$$v_{ph} = \frac{1}{\sqrt{C_{CPW} \cdot L_{tot}}} \tag{2.24}$$

$$Z_{cs} = \sqrt{\frac{L_{tot}}{C_{CPW}}} \tag{2.25}$$

In the range for typical impedances of 50 Ω the difference between normal conducting impedance and superconducting impedance amounts to approx 1 Ω. Figure 2.8 illustrates the normal and the superconducting impedance for different substrates materials.

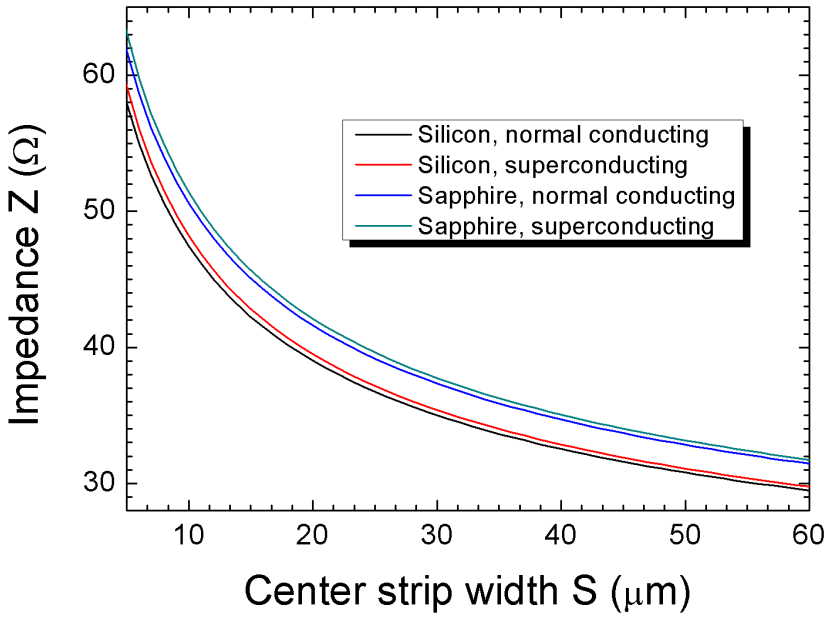

Figure 2.8: Comparison of normal and superconducting (@ 4 K) CPW impedance for Silicon and Sapphire with a fixed gap width W of 5 μm.

2.2.2 Attenuation

As in the case of a conventional CPW, also in the superconducting case only dielectric and conductor losses contribute to attenuation. Dielectric losses have already been treated in (2.16) on page 11. The closed form equation for the conductor losses

$$\alpha_c = \frac{R_{sm}}{8Z_c K^2(k) S(1-k^2)} \left\{ \ln\left(\frac{S}{\Delta}\frac{(1-k)}{(1+k)}\right) + k\ln\left(\frac{S}{k\Delta}\frac{(1-k)}{(1+k)}\right) \right\}$$

from equation (2.17) on page 11 also holds here.

The only difference to (2.17) relates to the complex wavenumber k_c in the modified surface impedance R_{sm} (2.18). One can use the two fluid model to explain this change.

The total conduction current density

$$\vec{J} = \vec{J}_s + \vec{J}_n$$

is assumed to consist of the superconducting current density $\vec{J}_s$ plus the normal current density $\vec{J}_n$.

Ohm's law

$$\vec{J}_n = \frac{n_n q^2}{m} \tau \vec{E} = \sigma_n \vec{E}$$

gives the normal current density.

We get the superconducting current density, written in phasor form in analogy to Ohm's law, with the help of the London equations:

$$\dot{\vec{J}}_S = \frac{1}{\mu_0 \lambda_L^2} \vec{E} = \frac{n_s q^2}{m} \vec{E} \Rightarrow \vec{J}_S = -\frac{i}{\omega \mu_0 \lambda_L^2} \vec{E} = -i\sigma_s \vec{E}$$

It is worth mentioning that both charge densities n_n and n_s depend on temperature. The total charge density amounts to $n = n_n + 2n_s$. Therefore, also σ_n and σ_s are temperature dependent. The temperature dependence of σ_s is already considered by the use of the temperature dependent London penetration depth (2.23). For σ_n the comparison to σ_s, with the fact that n is independent of T, gives a temperature dependence of $\left(\frac{T}{T_c}\right)^4$.

A new, complex conductivity

$$\vec{I} = \sigma \vec{E} = (\sigma_n - i\sigma_s)\vec{E}.$$

can be derived. This leads to the expression for the skin depth (2.19), and so (2.20) becomes

$$k_c^2 = \left(\frac{1}{\lambda_L}\right)^2 + 2i\left(\frac{1}{\delta_n}\right)^2$$

with

$$\begin{aligned} \delta_n &= \sqrt{\frac{2}{\mu_0 \omega \sigma_n}} \text{ and} \\ \lambda_L &= \sqrt{\frac{1}{\mu_0 \omega \sigma_s}}. \end{aligned}$$

Here, the meaning of λ_L as superconducting penetration depth is illustrated very clearly.

In order to calculate the conductor loss one finally needs the stopping distance Δ. As we have no data for the edge profile of our structures we assume $\theta = 90°$. Various values for Δ are listed in reference [18]. In Table 2.4 we see that the differences of the stopping distances and the London penetration depth given for Niobium at 4 K and 50 mK can be neglected, whereas the conductivity of the quasiparticles and, therefore, the skin depth vary much.

London penetration depth λ_0	"normal conductivity" $\sigma_n(T_c = 9.2\ \mathrm{K})$	layer thickness t	frequency f
47 ± 5 nm	$1.4{\cdot}10^9$ S/m [5]	200 nm	6 GHz

Table 2.3: Parameters used for the calculation the of the superconducting conductor losses.

temperature T	London penetration depth $\lambda_L(T)$	"normal conductivity" $\sigma_n(T)$	skin depth δ_n	stopping distance Δ
4 K	47,86 nm	$5{\cdot}10^7$ S/m	2.3 μm	1.4 nm
50 mK	47 nm	1.2 S/m	14 μm	1.41 nm

Table 2.4: Parameters derived from Table 2.3 used for the calculation of the superconducting conductor losses.

	conductor loss α_c		attenuation α	
design	Sapphire	Silicon	Sapphire	Silicon
Yale	0.032	0.034	0.032	0.62
design 1	0.017	0.018	0.017	0.61
design 2	0.017	0.012	0.011	0.60

Table 2.5: Attenuation of resonators $\alpha = \alpha_c + \alpha_d$, with α_d from Table 2.2.

2.2.3 Surface Impedance

From the results of the previous sections we get the formula for the surface impedance of a superconductor by a straightforward calculation. Using the surface impedance of a good conductor,

$$Z_S \approx (1+i)\sqrt{\frac{\omega\mu_0}{2\sigma}}$$

and inserting $\sigma = \sigma_n - i\sigma_s$, a binomial expansion gives

$$\begin{aligned} Z_S &= \frac{2}{\delta_s\sigma_s}\left(\frac{\lambda_L}{\delta_n}\right)^3 + i\omega\mu_0\lambda_L \\ &= \underbrace{2R_s\left(\frac{\lambda_L}{\delta_n}\right)^3}_{R_{Sf}} + i\omega L_S. \end{aligned} \tag{2.26}$$

R_s denotes the surface resistance of the normal conducting electrons which is reduced by (λ_L/δ_n) to the power of three in the superconducting case.

2.3 Microwave Resonators

Wallraff et al. performed an experiment in which a qubit is coupled to a microwave resonator [21]. In this chapter we present the basic theory of resonators adopted from [6] and [13].

Starting from a lumped element resonant circuit this section provides all important quantities needed for this work. We then proceed to distributed resonators and discuss the influence of superconductivity on the cavities.

2.3.1 Resonance Frequency

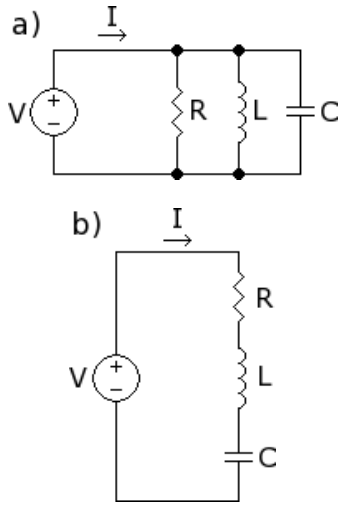

Figure 2.9: (a) parallel and (b) series lumped element resonant circuits

A series RLC resonant circuit, as shown in Figure 2.9(b) has the input impedance

$$Z_{in} = R + i\omega L - i\frac{1}{\omega C},$$

where resonance occurs if the imaginary part of the input impedance vanishes:

$$\omega_r L = \frac{1}{\omega_r C}$$

$$\Rightarrow \omega_r = \frac{1}{\sqrt{LC}} \text{ or } f_r = \frac{1}{2\pi\sqrt{LC}} \tag{2.27}$$

As shown in Figure 2.10 the phase shifts on resonance from +90° to -90°.

Concerning the resonance frequency some requirements have to be fulfilled for qubit experiments.

First, in order to be in the quantum regime one needs frequencies much higher than 1 GHz to satisfy the quantum condition: $hf \gg k_B T$ for temperatures of T = 30 mK.

Furthermore, the energy gap of Niobium is $\approx$ 3.8 $k_B T_C$ (with T_C = 9.2 K). For frequencies higher than 700 GHz one risks a collapse of superconductivity. Therefore, our resonators will be designed for frequencies around 6 GHz, the measurement range from 1 to 20 GHz.

For the parallel RLC resonant circuit (see Figure 2.9(a)) one calculates, in contrast to the serial circuit, the overall *admittance* $Y_{in} = \frac{1}{Z_{in}}$.

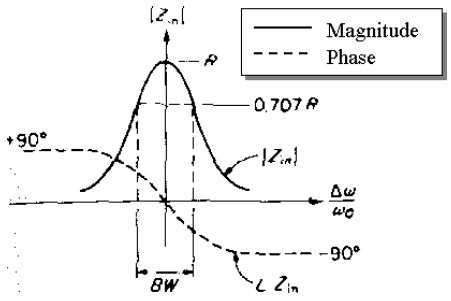

Figure 2.10: Z_{in} for a parallel resonant circuit

2.3.2 Quality Factor

The parameter Q, the *quality factor* of a resonant circuit, which is of high interest in this work, because it influences the rate of measurement in qubit experiments (see (2.30) in the next subsubsection), is defined as

$$Q = \omega \frac{\text{average energy stored}}{\text{energy loss/second}}.$$

The stored energy consists of the magnetic energy E_m and the electric energy E_e. These are equal on resonance.

For a serial and a parallel resonator the quality factor has to be calculated differently.

	serial resonator	**parallel resonator**
constant quantity	current I	voltage V
Average energies:		
power loss P_{loss} (dissipated by resonator)	$\frac{1}{2}\lvert I\rvert^2 R$	$\frac{1}{2}\frac{\lvert V\rvert^2}{R}$
magnetic energy E_m (in inductor)	$\frac{1}{2}L\lvert I\rvert^2$	$\frac{1}{2}L\lvert I_L\rvert^2 = \frac{1}{2}\lvert V\rvert^2\frac{1}{\omega^2 L}$
electric energy E_e (in capacitor)	$\frac{1}{2}C\lvert V_c\rvert^2 = \frac{1}{2}\lvert I\rvert^2\frac{1}{\omega^2 C}$	$\frac{1}{2}C\lvert V\rvert^2$
quality factor		
$Q = \omega_r\frac{2E_m}{P_{loss}}$	$\omega_r\frac{L}{R} = \frac{1}{\omega_r RC}$	$\frac{R}{\omega_r L} = \omega_r RC$

For practical reasons one can calculate

$$Q = \frac{f_{res}}{\Delta f}$$

by measuring the resonance frequency f_{res} and the full width at half maximum (FWHM) Δf (see Figure 2.10).

The FWHM can be determined by evaluating the frequencies where the transmission has fallen to 3 dB (3 dB = 1/2).[1]

2.3.3 Coupling to the Environment

In practice a resonance circuit is coupled to other circuits like the input line. This lowers the *internal quality factor* Q of the resonator to a *loaded quality factor* Q_L that can be expressed as

$$\frac{1}{Q_L} = \frac{1}{Q} + \frac{1}{Q_{ext}}. \tag{2.28}$$

[1] Originally the quality factor is defined for power. When calculating $20 \cdot \log \frac{V}{V_{in}}$ (like we do with the measured S-parameters, see section 2.4) one once again has a magnitude related to power.

The *quality factor of external circuits*

$$Q_{ext} = \frac{\omega C}{G_{ext}}$$

can be obtained for circuits coupled capacitively to the environment using

$$G_{ext} = \frac{2R_L C_{couple}^2 \omega^2}{1 + R_L^2 C_{couple}^2 \omega^2}$$

C_{couple} is the coupling capacity, R_L, the load resistance is 50 Ω for matched circuits. Three cases of coupling can be distinguished.

- $\frac{Q}{Q_{ext}} < 1$: undercoupled to feedline, $C_{couple} < \frac{\sqrt{\pi}}{\sqrt{2Q}\omega_r Z_0} \Rightarrow Q_L \approx Q$
- $\frac{Q}{Q_{ext}} = 1$: critically coupled to feedline
- $\frac{Q}{Q_{ext}} > 1$: overcoupled to feedline, $C_{couple} > \frac{\sqrt{\pi}}{\sqrt{2Q}\omega_r Z_0} \Rightarrow Q_L \approx Q_{ext}$

Coupling of a feed line to the resonator has the effect of lowering its resonant frequency [19]:

$$\omega_L = \frac{\omega_r}{\sqrt{1 + 2\frac{C_{couple}}{C}}} \tag{2.29}$$

From the above list one can see that Q_L can be tuned by varying the coupling capacitor. The rate of measurement is determined by the *decay rate*

$$\kappa = \frac{\omega_r}{Q_L} = \Delta f \tag{2.30}$$

of a photon in the cavity.

This is the predominant source of dissipation. Tnno have a rate of measurement of ≈ 1 MHz at ≈ 10 GHz one needs loaded quality factors of $Q_L \approx 10^4$. This means, a photon leaks out of the cavity in $T_r = 1/\kappa \approx 100$ ns.

The rate of measurements has to be faster than qubit decay rates.

2.3.4 Distributed Resonators

For microwave frequencies, lumped circuit elements are usually unattainable, so distributed elements are used. The reason is that the dimensions of the resonator are comparable to the wavelength. Therefore, voltage and current can not be averaged any more. In this thesis, we use resonators built of superconducting CPWs.

In Figure 2.11 two different resonator types are shown. A practical resonator that is often used in circuits (also in this work) is the transmission line, open circuited on either end, as shown in Figure 2.11(a). As indicated in this figure the electric and magnetic fields have to fulfill the boundary conditions. According to reference [18] such a resonator will behave as a parallel resonant circuit if the length amounts to $\lambda/2$, or a multiple of $\lambda/2$. In contrast,

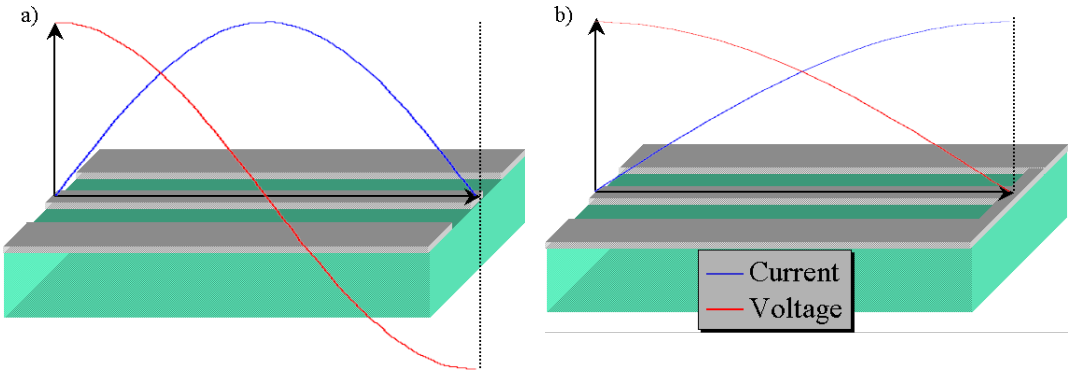

Figure 2.11: Ilustration of CPW resonators (a) $\lambda/2$ resonator (b) $\lambda/4$ resonator.

a short-circuited $\lambda/2$- resonator would behave as a serial circuit. The resonance frequency described in (2.27) can be derived by using the phase velocity v_{ph} (2.12) divided by two times the resonator length D

$$f = \frac{v_{ph}}{2D}. \tag{2.31}$$

A so called antiresonance can be achieved using a transmission line which is short circuited at one end with a resonance at $\lambda/4$, as shown in 2.11(b). In contrast to a short circuited $\lambda/2$ resonator this resonator behaves as a parallel circuit. This is due to the fact that a transmission line of length $\lambda/4$ behaves as an impedance converter and therefore transforms a serial circuit into a parallel circuit.

When capacitively coupling an $\lambda/2$ open circuited transmission line resonator that normally looks like a parallel RLC circuit near resonance at one end, it will look like a series RLC circuit near resonance. This is because the series coupling capacitor has the effect of inverting the driving point impedance of the resonator (like a quarter wavelength line does).

Coupling the $\lambda/2$ open circuited resonator on either side, it behaves as a parallel circuit.

The quality factor of a microwave resonator can be calculated by

$$Q = \frac{\beta}{2\alpha}, \tag{2.32}$$

where $\beta = \frac{2\pi}{\lambda} = \frac{2\pi f_r}{v_{ph}}$ is the propagation constant and α is the attenuation constant discussed in subsection 2.1.6 for normal conducting media and in subsection 2.2.2 for the superconducting case.

2.3.5 Superconducting Resonator

Finally, we will discuss the temperature dependencies of the resonance frequency and the quality factor of superconducting resonators.

From (2.24) and (2.21) one can directly observe that superconductivity influences the phase velocity v_{ph} through the kinetic inductance defined by (2.22). The kinetic inductance depends on the temperature dependent London penetration depth λ_L (see (2.23)). In Figure 2.12 the temperature dependence of the resonance frequency is shown. One can see that with constant length the resonant frequency decreases with increasing temperature.

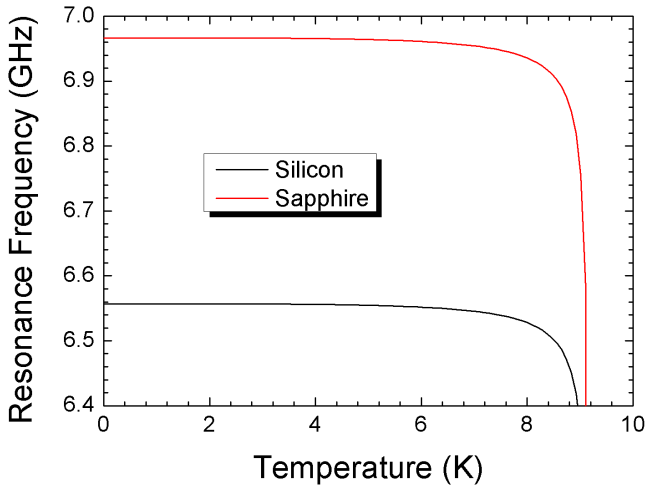

Figure 2.12: Dependence of the resonance frequency calculated with the kinetic inductance model for the Yale design on Silicon and Sapphire for a fixed length of 8.991 mm.

The quality factor Q is also temperature dependent, according to (2.32) it consists of the temperature dependent quantities β and α. In Figure 2.13 the quality factor dependence on temperature is shown for Silicon and Sapphire.

For Silicon one obtains quality factors of around 260. In our measurements the quality factor is one order of magnitude or more larger. The reason for this mismatching qualities could be that at lower temperatures the loss tangent is much lower than 0.004 (see Table 2.2). A value of around 0.00007 gives better matching results.

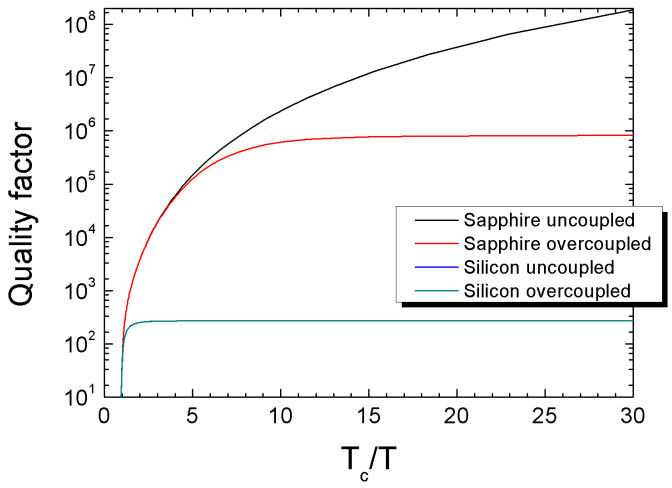

Figure 2.13: Dependence of the quality factor calculated with the kinetic inductance model for the Yale design on Silicon and Sapphire for a fixed length of 8.991 mm.

2.4 The Scattering Matrix

When dealing with high-frequency (hf) networks, voltages and currents (and the related impedances and admittances) are, in contrast to dc networks, abstract. For example, when the geometries can be compared to the wavelength, voltage and current distributions can not be averaged along the transmission line (see Figure 2.11 on page 21). The Scattering (S) matrix is a representation of a hf-network in accord with the ideas of incident, reflected, and transmitted waves. It provides a complete description of the network as seen at its ports by relating the voltage waves incident on the ports to those reflected from the ports.

The S-matrix is measured directly with a network vector analyzer. The scattering coeffi-

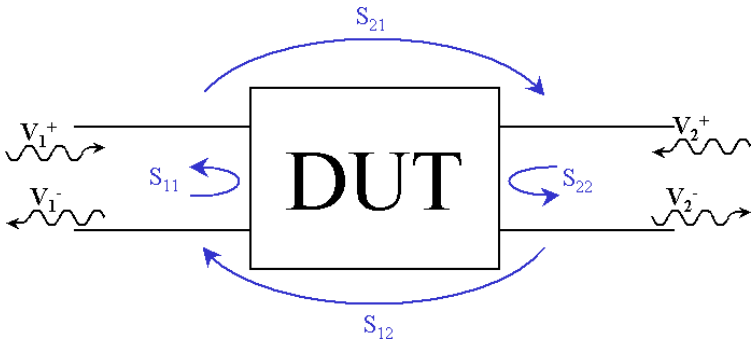

Figure 2.14: A two-port device illustrating incident, reflected and transmitted waves.

cient (e.g. the reflection coefficient) is determined by

$$S_{11} = \frac{V_1^-}{V_1^+}$$

The reflection parameters are defined with the other port terminated in matched loads to avoid reflection.

In general one can write for a two-port network

$$\begin{pmatrix} V_1^- \\ V_2^- \end{pmatrix} = \underbrace{\begin{pmatrix} S_{11} & S_{12} \\ S_{21} & S_{22} \end{pmatrix}}_{\mathbf{S}} \begin{pmatrix} V_1^+ \\ V_2^+ \end{pmatrix}$$

S_{21} and S_{12} are called transmission coefficients.

Two special cases can be considered to simplify the scattering matrix, the reciprocal and the lossless case. Reciprocal networks have no active devices, ferrites or plasmas. Not only the geometry, but also the transmission coefficients are symmetric: $S_{12} = S_{21}$. In matrix terms this can be written as $[\mathbf{S}] = [\mathbf{S}]^t$.

For lossless devices under test (DUTs) the power leaving the two-port must equal the total incident power. This leads to the following equations

$$\begin{aligned} |S_{11}|^2 + |S_{12}|^2 &= 1 \\ |S_{22}|^2 + |S_{12}|^2 &= 1 \\ S_{11}S_{12}^* + S_{12}S_{22}^* &= 1 \end{aligned}$$

The first equation shows that $|S_{11}| = |S_{22}|$. The matrix satisfying this conditions is a unitary matrix $[\mathbf{S}]^* = ([\mathbf{S}]^t)^{-1}$

The reader may be interested in table 4.2 in [18]. This table gives conversion formulas between various two-port network parameters like S and Z.

3 Designs Procedure for the Resonators

In this thesis two substrate materials, namely Sapphire and Silicon, were used, as mentioned in the previous chapters.

The *Sapphire* substrates had already been used by Andreas Emmmert [5] to fabricate a superconducting beam splitter or hybrid ring. If it is possible to realize both resonator and beam splitter on the same chip new measurements e.g. vacuum fluctuations in the resonator will be possible. (This idea is presented in [11])

The production of nanostructured qubits by means of electron beam lithography is much more straight forward on *Silicon* substrates because of the high conductivity of Silicon at room temperature. Hence, we fabricated resonators on Silicon for the future experiment of placing a qubit in the resonator.

The (effective) dielectric constants and the (effective) thinknesses of the substrates were mentioned in subsection 2.1.2. On top of the substrates the resonators were deposited with Niobium, which is weakly sensitive to an applied magnetic field (the upper critical field B_{C2} is around 2 T) and has only a very small amount of quasiparticles at the future operation temperature of 50 mK due to a high critical temperature of 9.2 K.

For the design of the resonators you have to decide on the following parameters:

1. substrate material (Sapphire or Silicon)
2. gap W between center strip and ground planes
3. resonance frequency
4. coupling capacitance

3.1 Resonator

After choosing the substrate material and the width of the gap W, the center strip width S is calculated for Z_{cs} to be 50 Ω, to match the resonator structure to the coaxial cables and avoid reflections. The approximations (3.1) and (3.2) of equation (2.25) for CPWs with infinite box height H_1 are used for calculating the center strip width S corresponding to the chosen gap width W. In order to calculate the center strip width we used approximations for Sapphire

$$S = \begin{cases} \frac{W+0.3308}{0.492} & \text{if } W < 51 \\ \frac{W+0.8908}{0.4886} & \text{if } W > 51 \end{cases} \tag{3.1}$$

and for Silicon

$$S = \begin{cases} \frac{W+0.3742}{0.5908} & \text{if } W < 51 \\ \frac{W+0.9579}{0.6006} & \text{if } W > 51. \end{cases} \tag{3.2}$$

The calculated values are shown in Table 3.1. The "Yale" design was adopted from reference [6]. For simplicity, values evaluated from (3.1) and (3.2) were rounded to values divisible by 5. Therefore, most values in Table 3.1 are equal for Silicon and Sapphire substrates. Design 2 was only designed for Sapphire substrates.

design	gap width W (μm)	center strip width S (μm)
Yale	5	10
design 1	10	20
design 2	25	45

Table 3.1: Description of designs with corresponding geometries

The resonator length is evaluated from (2.24) and (2.31). Here, again an approximation (3.3) is used.

$$\varepsilon_{eff} = \begin{cases} 6.007S^{-0.012} & \text{for Sapphire} \\ 6.853S^{-0.0148} & \text{for Silicon} \end{cases} \tag{3.3}$$

The values in Table 3.2 result from the presented procedure. While taking the approximated values for the design an exact calculation gives values slightly deviating from the approximation.

substrate material	permittivity ε_r	design	permittivity ε_{eff} approximation	exact calculation
Sapphire	10.34	Yale	3.45	5.67
		design 1	3.42	5.67
		design 2	3.39	5.66
Silicon	11.8	Yale	4.06	6.45
		design 1	4.02	6.45

Table 3.2: Effective permittivities corresponding to the designs

The length of the resonator was chosen to get the desired resonance frquency for the resonator.

3.2 Coupling Capacitances

The coupling capacitances were adopted from the design of Frunzio [6].

The undercoupled resonator on the left hand side of Figure 3.1 has a gap width g of 4 μm serving as a capacitance. The appropriate capacitance for design 1 is linearly scaled with the ratio of the gap widths W. So a gap g of 8 μm is obtained.

On the right hand side of Figure 3.1 the capacitance for the overcoupled resonator in the Yale design is shown. The inner conductor is divided into two stripes of length ≈ 100 μm

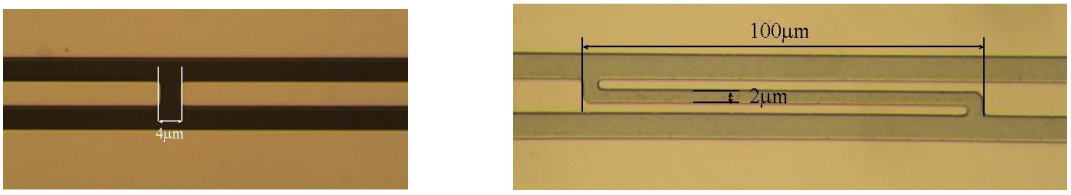

Figure 3.1: Coupling capacitors used in the paper of Frunzio el al [6].

each being 4 μm wide (”fingers”) and a gap of 2 μm between those two stripes. The capacitance of the overcoupled resonator of design 1 is done by enlarging the length and the number of the fingers. The length is scaled linearly compared to the Yale design, as was done in the undercoupled case.

For design 2 only a slightly overcoupled resonator was fabricated. Here, the length of the fingers was enlarged, their number remained constant compared to the overcoupled resonator of design 1.

Table 3.3 gives an overview of the used dimensions. The capacitance values were calculated using Xic[1].

design	coupling	capacitance (fF)		undercoupled gap width	overcoupled	
		Sapphire	Silicon	g (μm)	# fingers	length (μm)
Yale	undercoupled	0.58	0.69	4		
	overcoupled	6.2	7.1		2	100
design 1	undercoupled	1.1	1.2	8		
	overcoupled	21	24		3	200
design 2	slighty overcoupled	31			3	350

Table 3.3: Overview of the dimensions and values of the coupling capacitances.

Due to the coupling capacitors the resonance frequency differs from the one the resonators were designed for (see (2.29)). The modified resonance frequencies and an overview of the designed resonators are listed in Appendix A.

3.3 Connectors

In the design of the measurement box (refered to as ”Gold plated box”) SMA Connectors 32K724-600S3 SMA from Rosenberger[2] were used. The flat center conductor pin of the connector (diameter 510 μm) is embedded in a teflon dielectric of diameter 2.18 mm. The pin length, not covered by dielectric on the inner side of the box is 1 mm. The connector can be plugged to a cable with SMA male connectors.

[1] www.wrcad.com
[2] www.rosenberger.de

In order to have a spatial tolerance at the connection from the center conductor of the connector to the one of the resonator structure the inner strip of the tapering structure was designed to have a diameter of 800 μm.

For this dimension no matching to 50 Ω is possible within CPW technology. In order to minimize the effect of mismatch, the dimensions of the gap were adapted to the width of the dielectric of the connector. This avoids a parasitic reactance produced by discontinuities in geometry.

4 Fabrication and Measurement Setup

4.1 Fabrication Process

All resonators were fabricated in the cleanroom facilities at the Walther-Meißner-Institut.

Two optical masks with several different resonator geometries were designed within this diploma thesis and ordered from ML&C[1]. The relevant dimensions and design rules of the resonators are given in chapter 3 on page 27. An overview of the masks is found in Appendix B on page 73.

Figure 4.1 shows the different fabrication steps.

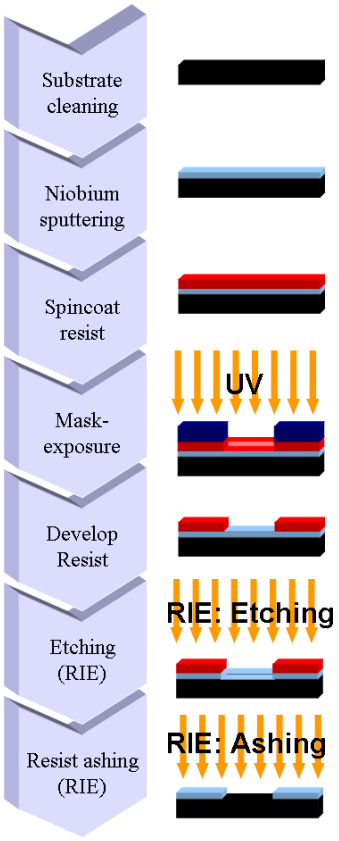

Figure 4.1: Overview of the Niobium CPW fabrication process.

[1] www.mlc-jena.de

Cleaning the substrates

The substrates were ultrasonic-cleaned in each of the following solvents:

- Acetone technical
- Acetone p.a.
- Isopropanol

Sputtering Niobium

After the cleaning process, the substrates are ready to be sputtered with Niobium. They are screwed into a specially designed carrier in order deposit Niobium on both sides of the substrate for CBCPW, without scratching the Niobium layer.

The carrier is then placed in the sputtering chamber and positioned in front of the desired target, in our case Niobium.

The sputtering is done with the following parameters:

- process pressure: $\approx 2.7 \cdot 10^{-3}$ mbar
- argon flow rate: 10 sccm/min
- power: 200 W
- duration: 5 min + presputtering 60 s

During presputtering the power stabilizes. With these sputtering parameters we achieve a layer thickness of 200 nm.

Spincoat the resist

In the cleanroom the substrate coated with Niobium is cleaned again as described above, in order to remove eventually captured particles (e.g. dust). After this, the sample is spincoated with photo resist (AZ 5214E, Microchemicals[2]). The spin coating is done with 4000 rpm for 40 seconds, resulting in a resist thickness of 1.4 μm.

Afterwards, the sample is baked for 120 seconds at 110 °C (soft bake) to improve the adhesion of the resist.

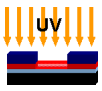

Mask exposure

The UV-exposure is done with the mask aligner (MJB3, Karl Süss GmbH). The mask is carefully cleaned under flowing acetone and isopropanol and placed in the mask holder. The substrate is aligned with the desired resonator structure.

We used the high precision modus to have optimum accuracy of the structure on the sample. The samples are exposed with UV radiation for 4 seconds.

[2] www.microchemicals.com

Develop Resist

The areas exposed to UV light are then removed in a developer - water solution for 2 minutes (developer : H_20 = 1 : 1).

After development, any developer remaining on the sample is washed away in a water bath. At the end of this step the coarse structures of the resonator are clearly visible by eye. The samples were always checked under the microscope to see if the optical lithography process was successful and all structures were developed completely. If we were not satisfied with the result the sample was cleaned, spincoated and exposed again.

Etching and Ashing in RIE

We used an "Oxford Plasma Lab 80 Plus" Reactive Ion Etching machine. The frequency for producing the Ion-Plasma is 13.56 MHz. The other parameters are:

parameters	physical etching	ashing
duration:	2:00 min	3:00 min
flow rates:		
Ar:	10.0 sccm/min	0 sccm/min
SF_6:	20.0 sccm/min	0 sccm/min
O_2:	0 sccm/min	50.0 sccm/min
N_2:	0 sccm/min	
He backing:	10.0 sccm/min	
RF forward power:	100 W	100 W
ICP forward power:	50 W	0 W
chamber pressure:	15 mTorr	30 mTorr
temperature:	20 °C	

Table 4.1: Parameters used in the RIE process.

We decided to go for physical etching due to an improvement of the resolution of our structures in contrast to the also available chemical etching.

After the last step the resonator is cooked in acetone to remove remaining resist and is cleaned again. Now the device is ready for testing and mounted into the measurement setups.

4.2 Measurement Setup

The fabricated devices (Device under test, DUT) were tested in different boxes in the cryostat (described in detail in Figure 4.3):

The PCB box was designed by Stefan Nimmrichter in his internship at the Walther-Meißner-Institut. Here, the resonators are glued to a PCB and connected via bonding wires.

The Hybrid box was designed and used by Andreas Emmert, a former Diploma student designed originally for CPW hybrids [5]. The connection between the connector pins and the taperline was established with a droplet of silver glue.

Gold plated box This box was designed especially for the measurements of the CPW resonators. It was produced of oxygen free copper and covered with gold to improve the connection to ground. The resonators are put into a carefully milled recess.

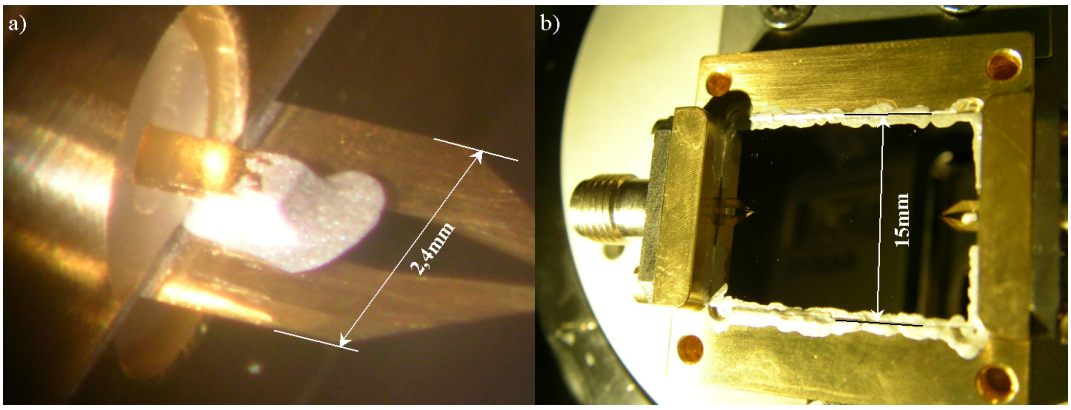

Figure 4.2: Connecting with silver glue (a) on connector (b) grounding on edges.

For the connections to the taper lines of our resonators Rosenberger stripline SMA-Connectors (section 3.3) were used. The advantage of this decision is, that we do not have to use bonding wires on a PCB. For better electronic contact, we put a droplet of silver glue between the connector pins and the taperline. For putting the silver glue on the small pin, the microscope of the bonding machine was used. A cold light source had to be used, instead of the much heat producing lamp of the bonding machine, to glue the devices, since silver glue hardens very fast. The ground planes of the DUT were connected to the box, by putting silver glue all over the edges of the structure to the box (Figure 4.2).

After checking for shorts the sample was connected to the coaxial cables of the cryostat (Figure 4.4).

The measurement setup is shown in detail in Figure 4.3.

A Labview program controls the settings (like start, stop-frequency) of the Network Vector Analyzer (NVA) and is able to record data at selected temperature steps. The magnitude and the phase of transmission and reflection measurements were extracted from the calibrated data returned by the NVA.

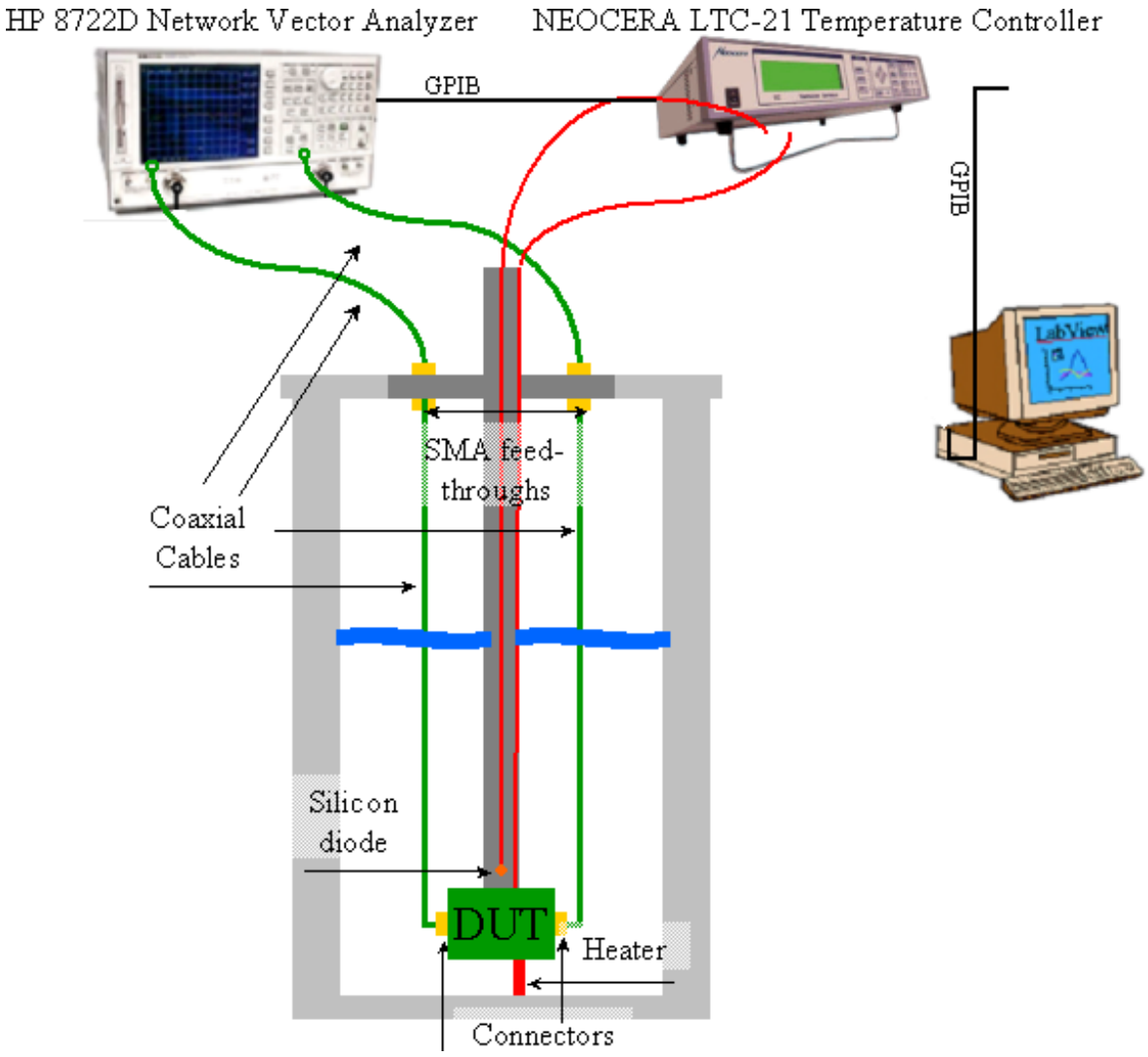

Figure 4.3: Measurement setup with the cryostat.

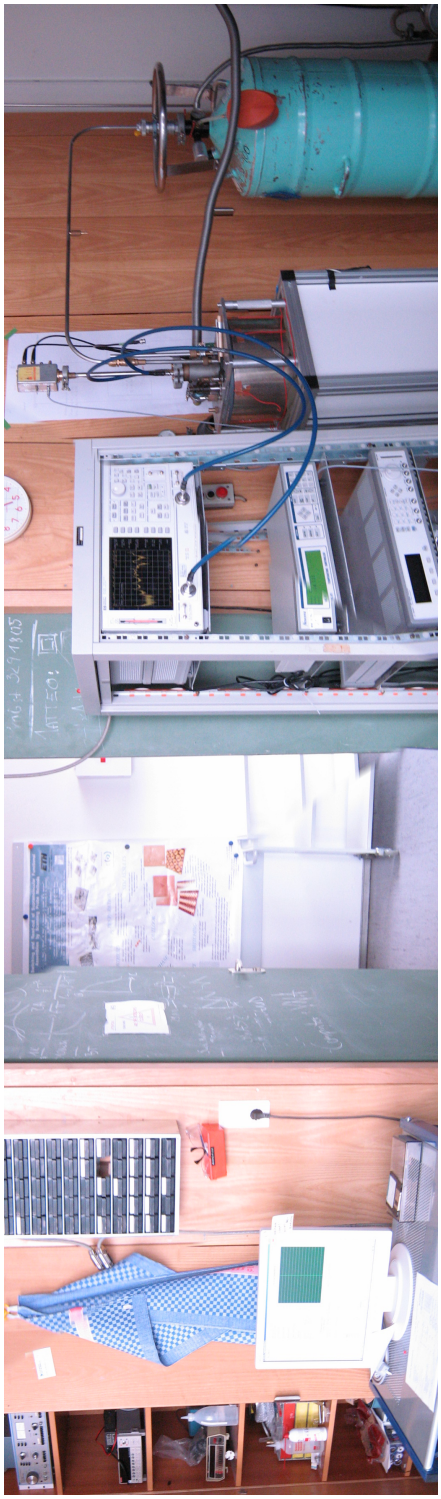

Figure 4.4: Picture of the measurement setup with PC (with LabView) on the left, helium can on the right and RT measurement devices in between.

4.3 Calibration

In order to eliminate systematic errors resulting from mismatches, reflections, crosstalks etc. in the NVA and feed cables, the setup is calibrated with known calibration standards. These calibration standards are connectors including a short, an open, a broadband load termination and a through, matched to 50 Ω. When starting this work, the calibration techniques were already well established (see [12], [5], here also further information about temperature dependent calibrations can be found). All calibrations were performed at room temperature.

We used two different calibration schemes for transmission and reflection.

In *transmission*, a 50 Ω through adapter was connected in between the feedlines. The NVA then provides a response calibration function where the calibration data is recorded. In measurements, the measured data is then normalized to the calibration data. This calibration is very simple, but eliminates only two of twelve possible errors.

In most measurements we only calibrated the feed cables connected to the cryostat. For phase measurement we decided to record data where the cables in the cryostat were also calibrated. At resonance all power is transmitted and the output power should reach 0 dB.

Reflection measurements were calibrated with 1-port calibration. Therefore, we connected the cables in the cryostat with an 50 Ω adapter. One of the feed throughs on top of the cryostat was connected to the NVA (the feed cables to the cryostat are numbered because one should always use the same cables for reflection measurements) the other feed through was terminated with a short, an open and a broadband load. The NVA provides a routine to calibrate the reflection measurement with all these standards. While measuring the feed through not connected with a feed cable has to be terminated with the broadband load.

5 Measurements

The first part of this chapter deals with problems and failures that occured in our measurements, the second part presents the successful experiments in detail. The measurements were done using all three designs of resonators described in chapter 3 in the order design 1, Yale design, design 2.

5.1 First Experiments

This section is dedicated to the first measurements, according to Murphy: "Everything that can go wrong goes wrong." Most of them were done using equipment already available at the Walther-Meißner-Institut before the gold plated box was fabricated (see section 4.2).

Here, an overview of the measurement results and possible explanations as to why these experiments failed are given. All measurements were done on Sapphire.

name	design	W [μm]	S [μm]	length [mm]	frequency [GHz]	capacitance	value	substrate material
R20	Yale	5	10	9.759	6.4174	undercoupled	6.2 fF	Sapphire

Table 5.1: Description of the resonator R20 on Sapphire.

The resonator R20 was first measured in the Hybrid box, where we observed different peaks with quality factors from 30 to 130 at 4 K. The quality factors were not increasing when cooling the resonator to 1.5 K. We could not find matching harmonics for any of these peaks. An evaluation of the phase data showed no phase shifts. Another measurement in the gold plated box showed no peaks in the spectrum.

name	design	W [μm]	S [μm]	length [mm]	frequency [GHz]	capacitance	value	substrate material
R22	Yale	5	10	9.515	6.5819	undercoupled	0.58 fF	Sapphire

Table 5.2: Description of the resonator R22 on Sapphire.

R22 which is of the same geometry as R20 but with different resonator length was measured in the Hybrid box. We saw a peak shifted approximately by 0.14 GHz in comparison to R20 (see Figure 5.1). We were not sure whether this is the resonance peak, because no phase shift was observed.

R24 in the Gold plated box showed peaks with quality factors from 20 to 100. We concluded that these peaks are no resonances because no change in phase occurred in the phase

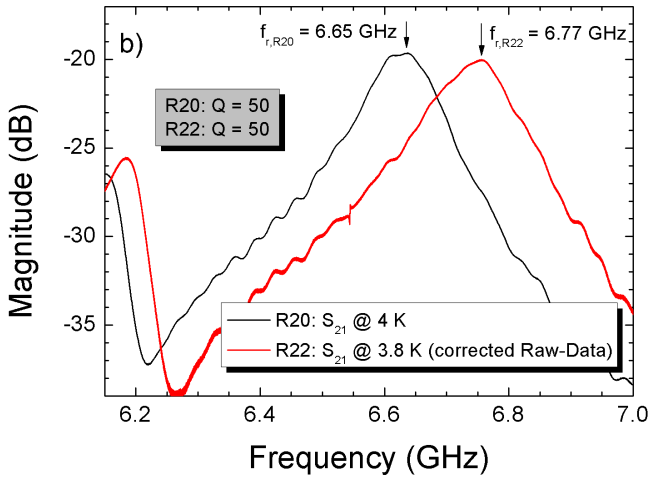

Figure 5.1: Transmission S_{21} of R20 and R22 at 4 K in the hybrid box. Since the recorded data from R22 was uncalibrated a level of 20 dB is added to the data.

name	design	W [μm]	S [μm]	length [mm]	frequency [GHz]	capacitance	value	substrate material
R24	Custom 1	10	20	9.8	6.403	undercoupled	1.1 fF	Sapphire

Table 5.3: Description of the resonator R24 on Sapphire.

measurement.

One reason why we saw resonance peaks that could not be identified with resonators and had low quality factors could be the different fabrication techniques used by our group and the group in Yale. Frunzio [6] uses a lift off process, our group, in contrast, uses a RIE process that could lead to the observed very sharp edges of our structures (an electron-beam micrograph is shown in Figure 5.2). At these edges the electric field diverges.

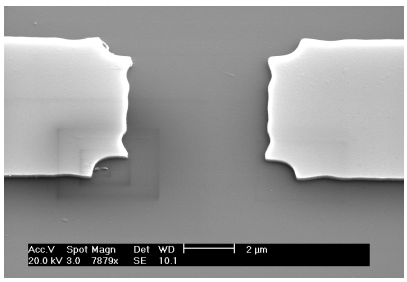

Figure 5.2: Coupling Capacitance of R20 (same as Figure 3.1 on page 29)

name	design	W [μm]	S [μm]	length [mm]	frequency [GHz]	capacitance	value	substrate material
R41	Yale	5	10	9.759	5.85	overcoupled	6.2 fF	Sapphire

Table 5.4: Description of the resonator R41 on Sapphire.

R41 was designed for and measured in the probing station installed at the Walther-Meißner-Institut which allows fast measurements down to below 4 K for frequencies up to 20 GHz. At 4 K no change in the spectrum compared to room temperature was visible. The resonator was additionally tested at room temperature in a probing station at the Institute for High-Frequency Engineering of the Technical University of Munich. Also here the structures showed insulating behavior. With high probability the Wolfram probes of the probing station are not able to connect to the Niobium, as the latter is insulated due to an oxide layer.

After having no success in a probing station, we bonded R41 in the PCB box. We clearly saw a peak at 6.16 GHz at 4 K with an insertion loss of -15 dB, that is not visible at higher temperatures. We are not sure whether this is the desired resonance peak as we have no phase data to verify the result. In addition the magnitude is much smaller than what we would expect in the case of a resonance. The peak is broad and has a quality factor of around 60. With this coupling capacitance geometry Frunzio et al. [6] measured quality factors of about 5×10^3 at 4.2 K.

5.2 Measurements – Design 1

This section presents the measurements on *overcoupled* resonators for design 1. Overcoupled resonators are expected to have a smaller quality factor, because of a larger coupling to the environment. At first Silicon was used as substrate material, later on Sapphire. Therefore, a comparison between Silicon and Sapphire is given for the resonator R25. After this, R25 is compared to R27, a resonator with the same geometry except for the resonator length.

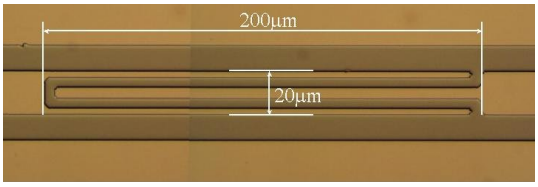

Figure 5.3: overcoupled capacitance of R25

5.2.1 R25 on Silicon

name	design	W [μm]	S [μm]	length [mm]	frequency [GHz]	capacitance	value	substrate material
R25	design 1	10	20	9.8	6.003	overcoupled	24 fF	Silicon

Table 5.5: Description of the resonator R25 on Silicon.

The capacitance and the resonance frequency in Table 5.5 are calculated for Silicon. Although the structure was designed for Sapphire, it is also 50 Ω matched for Silicon (see Table 3.1 on page 28). This matching is valid up to a gap size of 15 μm. Also the tapering is the same, since the taper structures could not be matched to 50 Ω at all and so just the geometries of the connector and the taper were matched (see section 3.3).

When cooling down below the superconducting transition temperature of Niobium, we observed a very sharp peak in the transmission spectrum at 6.15 GHz (see Figure 5.4) with a quality factor of about 1100.

Detailed measurements of reflection, harmonics and phase of the resonator are presented in the following Figures. In Figure 5.5 one can see the transmission and reflection parameters near the resonance peak. Surprisingly, the quality factor of reflection is about 10 times larger than in the case of transmission.

The harmonics in Figure 5.6 are almost exact multiples of the fundamental resonance. The first harmonic mode at 12.3 GHz looks distorted. Perhaps other resonances (e.g. the ”gold box mode” at 11.9 GHz) are interfering with this mode. The second harmonic at 18.4 GHz is still sharp and has a quality factor of 50.

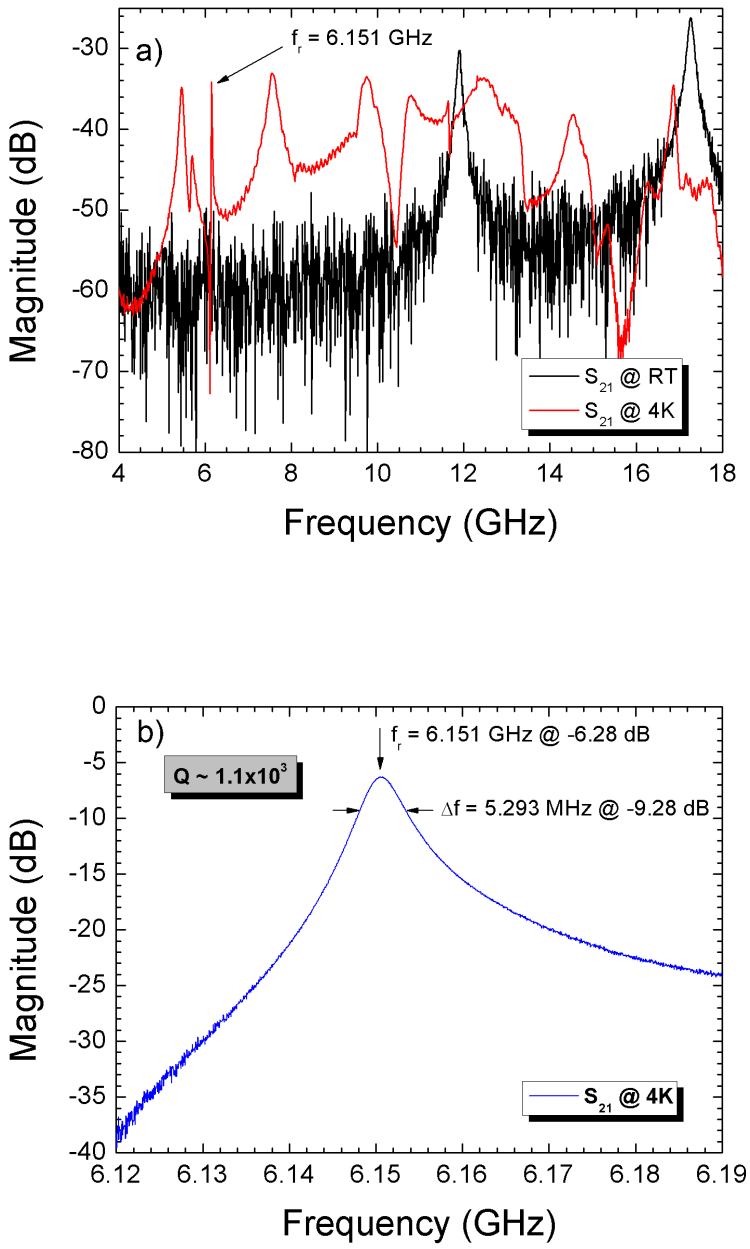

Figure 5.4: Transmission S_{21} of R25 on Silicon (a) at different temperatures (b) enlargement of transmission at resonance at 4 K.

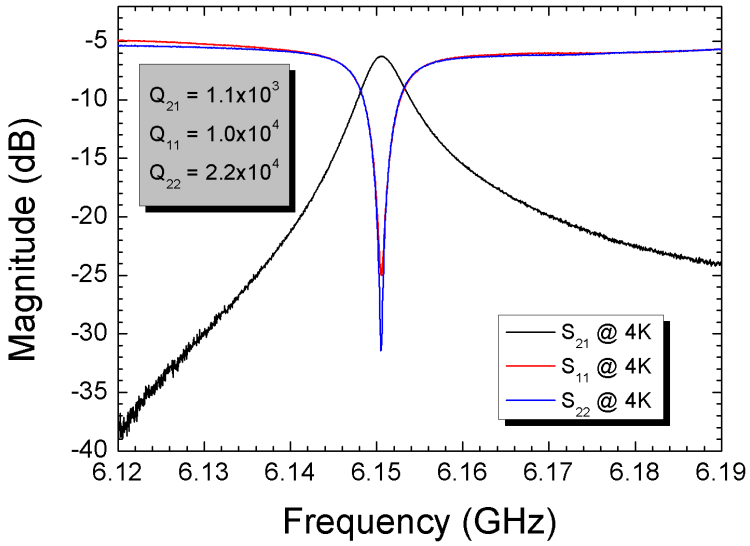

Figure 5.5: Transmission S_{21} and reflection S_{22} and S_{11} of R25 on Silicon at 4 K.

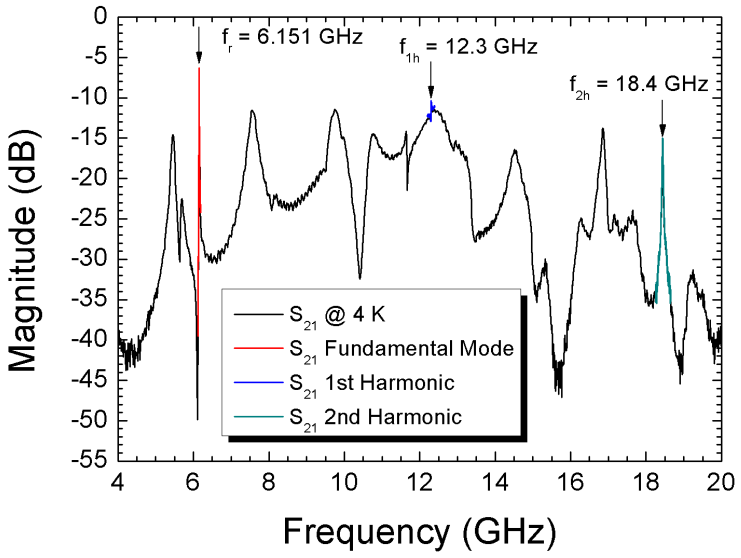

Figure 5.6: Transmission S_{21} of R25 on Silicon at 4 K with a fundamental resonance at 6.15 GHz and marked harmonics at 12.3 GHz and 18.4 GHz.

The advantage of using a vector analyzer (and not a scalar one) is the ability not only to measure the amplitude of a signal, but the whole complex signal including phase information. As described in section 2.3 one should observe a phase shift of 180° (from +90° to -90°) when sweeping the frequency through the resonance. In Figure 5.7 the phase shift at the resonance frequency is shown.

As one can see from the lower graph, the maximum of the amplitude is above 0 dB because the superconducting resonator has less attenuation than the normal conducting 50 Ω adapter used for calibration.

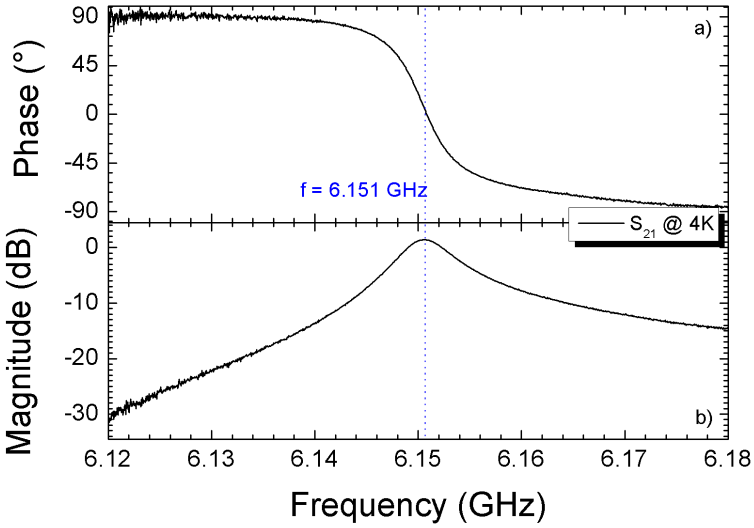

Figure 5.7: Transmission S_{21} of R25 on Silicon at 4 K: Phase shift (a) and magnitude (b) at resonance. The data was recorded with calibration including the cables inside the cryostat.

In Figure 5.8 the transmission of R25 is depicted for different input powers. Starting at around -23 dBm the resonance peak becomes distorted with increasing output power of the NVA. This effect was reported by Frunzio [6].

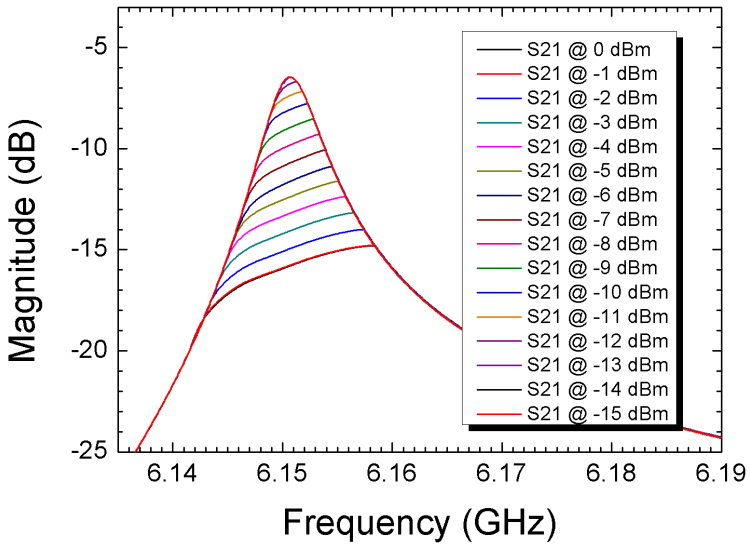

Figure 5.8: Transmission S_{21} of R25 on Silicon: Distortion of resonance peak with increasing input power.

5.2.2 R25 on Sapphire

name	design	W [μm]	S [μm]	length [mm]	frequency [GHz]	capacitance	value	substrate material
R25	design 1	10	20	9.8	6.402	overcoupled	21 fF	Sapphire

Table 5.6: Description of the resonator R25 on Sapphire.

For R25 we expect a difference of the resonance frequency between Silicon and Sapphire of 0.4 GHz. In Figure 5.9 a shift of 0.6 GHz can be observed. The quality factor on Sapphire (around 800) is lower than on Silicon (1000).

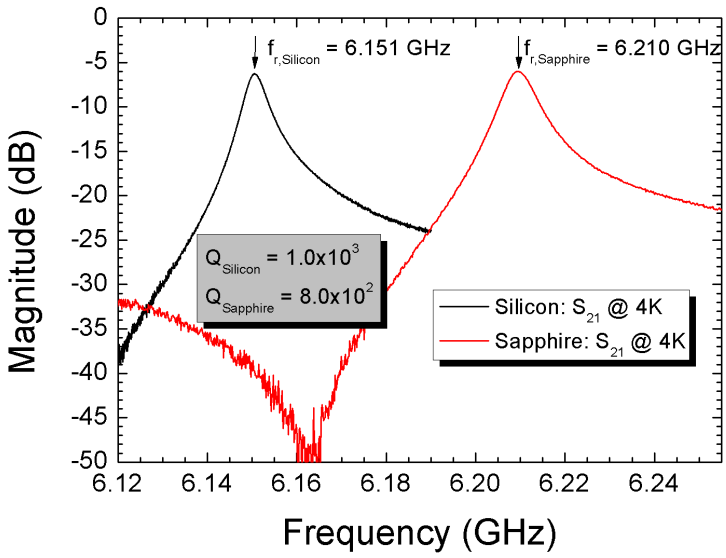

Figure 5.9: Comparison of transmission S_{21} of R25 on Silicon and Sapphire.

5.2.3 R27 on Silicon

R27 is similar to R25 except for the length. Thus the calculated resonance frequency is increased by 0.15 GHz in comparison to R25 to 6.156 GHz.

name	design	W [μm]	S [μm]	length [mm]	frequency [GHz]	capacitance	value	substrate material
R27	design 1	10	20	9.555	6.156	overcoupled	24 fF	Silicon

Table 5.7: Description of the resonator R27 on Silicon.

In Figure 5.10 the resonance peaks of R25 and R27 are shown, recorded at 4 K. The peaks are separated by 0.18 GHz, the quality factors at this temperature are almost equal and included in the graphs.

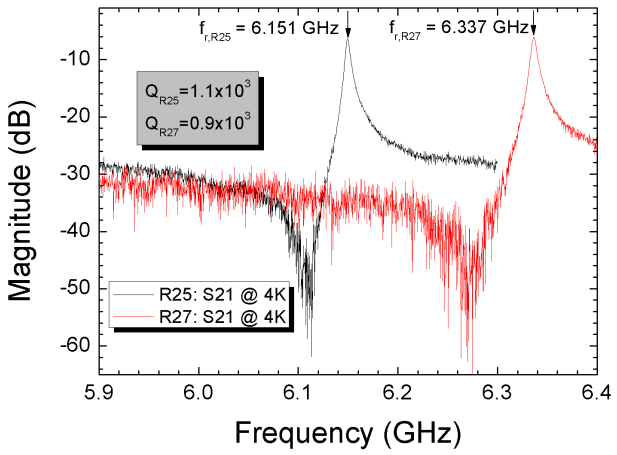

Figure 5.10: Comparison of transmission S_{21} of R25 and R27 on Silicon at 4 K.

Figure 5.11 shows the change of resonance frequency and quality factor with increasing temperature. By coming nearer to the transition temperature, the resonance frequency and the quality factor decrease (see subsection 2.3.5). The step at 4.3 K, in the resonance frequency vs. temperature graph can be explained the following way: all measurements described before were measured at 4 K. For the temperature resolved measurement the liquid Helium is pumped to 1.5 K. Measurements were recorded during warm-up. As soon as the liquid helium is vaporized we saw the jump, due to a change in the dielectric constant between liquid and gaseous Helium. The jump of 15.312 MHz can be explained with a dielectric constant of liquid Helium of 1.0047. In the RIE process we always etched into the Silicon Oxide layer in the gap between the inner strip and the ground plane. This could possibly explain the deviation between the experimental value and the value documented in literature (1.05 [8]) of the dielectric constant of liquid Helium. Theory predicts the measured result that the quality factor does not change.

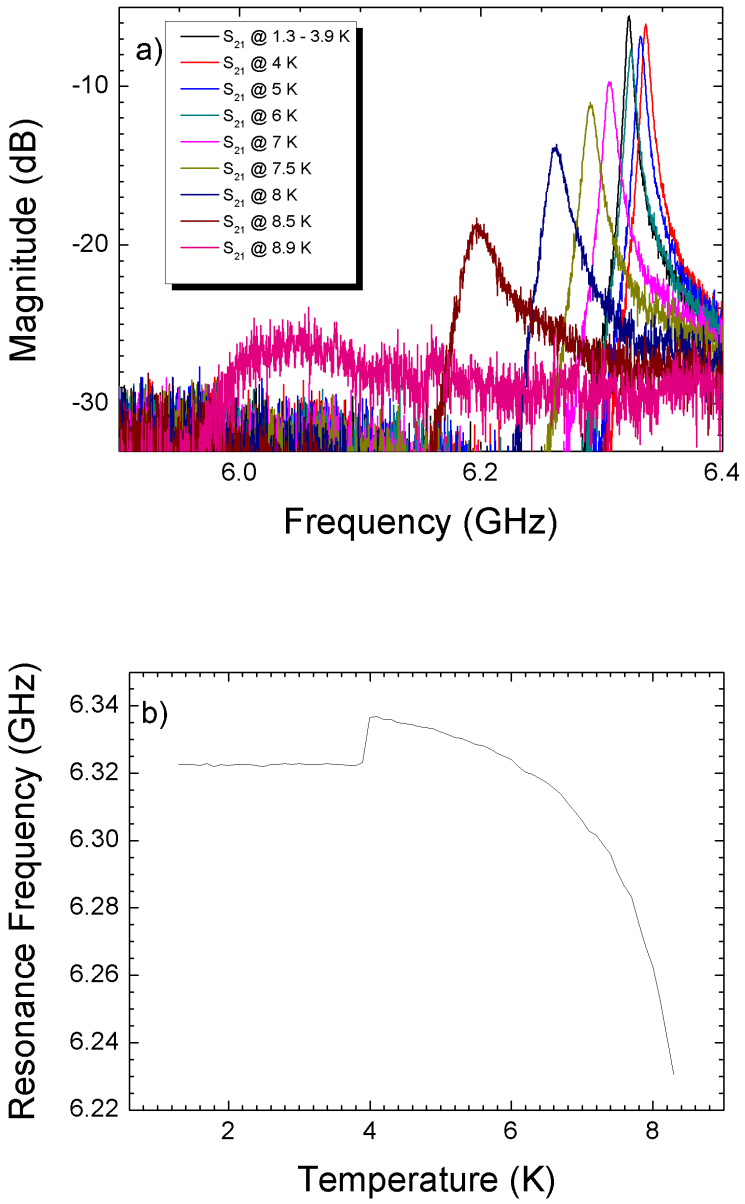

Figure 5.11: (a) Transmission S_{21} of R27 on Silicon at different temperatures, (b) dependence of resonance frequency on temperature.

5.3 Measurements – Yale Design

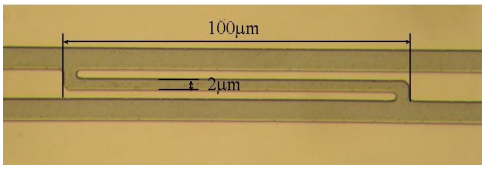

Figure 5.12: Overcoupled capacitance of R21.

Measurements based on the Yale design are done on R21, a resonator designed for a resonance frequency of 5.85 GHz, on Silicon and Sapphire. It is, as well as design 1, overcoupled to the environment (see Figure 5.12). R41 for the probing station (see section 5.1) has the same geometry.

5.3.1 R21 on Silicon

name	design	W [μm]	S [μm]	length [mm]	frequency [GHz]	capacitance	value	substrate material
R21	Yale	5	10	9.759	6.0166	overcoupled	7.1 fF	Silicon

Table 5.8: Description of the resonator R21 on Silicon.

At 4.2 K we observed a quality factor of 6000. After cooling to $\sim$ 1.4 K the quality factor increased to a value of about 15000. The measurement is shown in Figure 5.13. When cooling to 17 mK in the new cryostat installed at the Walther-Meißner-Institut no further increase in quality was visible. This is expected, because an increase in the internal quality factor influences the overall quality factor weakly in the case of overcoupled resonators (see subsection 2.3.3).

In subsection 2.3.3 on page 19 it was shown that a quality factor of 10^4 is required to perform experiments with qubits. With R21 this condition is fulfilled. With a quality factor higher than this value the readout becomes more difficult, because the photon lifetime in the cavity is proportional to the quality factor and the photon would stay in the cavity for too long (see (2.30) and following).

When measuring the reflection around the resonance peak, a strange behavior of the resonance dip can be seen (Figure 5.14). Although the S_{21} resonance has a quality of ten thousand, the quality in reflection is lower. This is in disagreement with the observation made on R25 (Figure 5.5 on page 44) where the quality in reflection exceeds the quality factor in transmission.

In Figure 5.15 the full spectrum with the first and second harmonics is shown.

The frequencies of the harmonics again lie almost exactly (the deviation is at the third digit) at multiples of the first resonance. The first harmonic again is not as clear as the fundamental resonances and the second harmonic has a quality factor $\approx$ 2000.

We also observed a distortion of the resonance peak with increasing output power above -17 dBm (see Figure 5.16).

Figure 5.17 shows the increase of the resonance frequency and the quality factor with decreasing T. The jump at 4.3 K can be attributed to liquid He in the box.

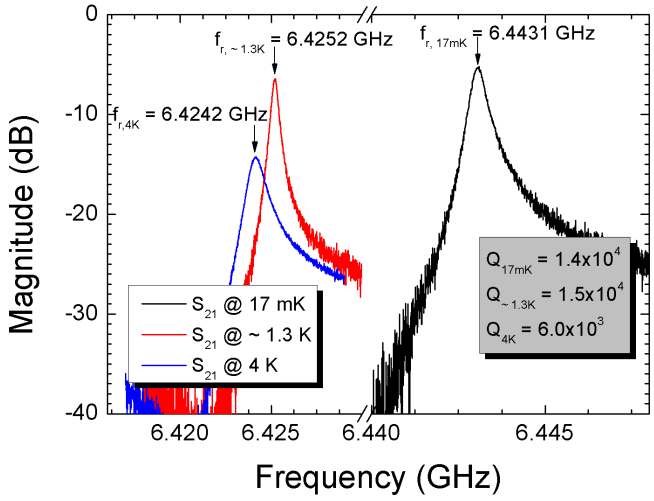

Figure 5.13: Transmission S_{21} of R21 on Silicon at the resonance frequency at 4 K, below 1.3 K and at 17 mK. Comparison of quality factors.

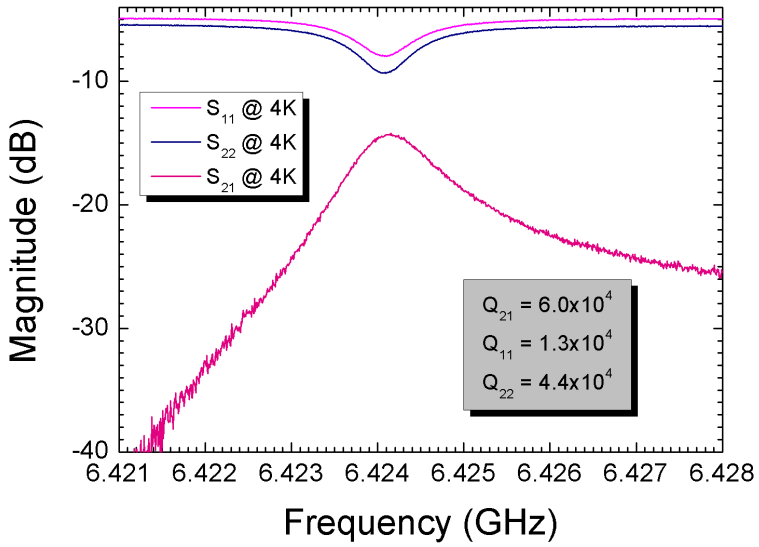

Figure 5.14: Transmission S_{21} and reflection S_{22} and S_{11} of R21 on Silicon at 4 K.

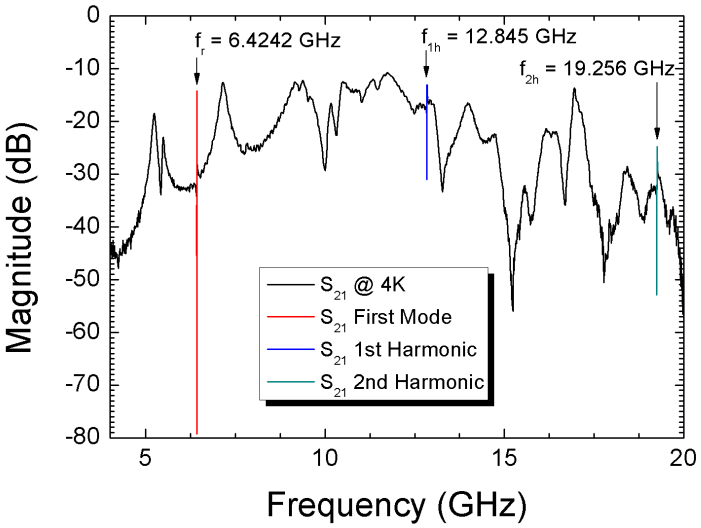

Figure 5.15: Transmission S_{21} of R21 on Silicon at 4 K with fundamental resonance at 6.42 GHz and marked harmonics at 12.85 GHz and 19.26 GHz.

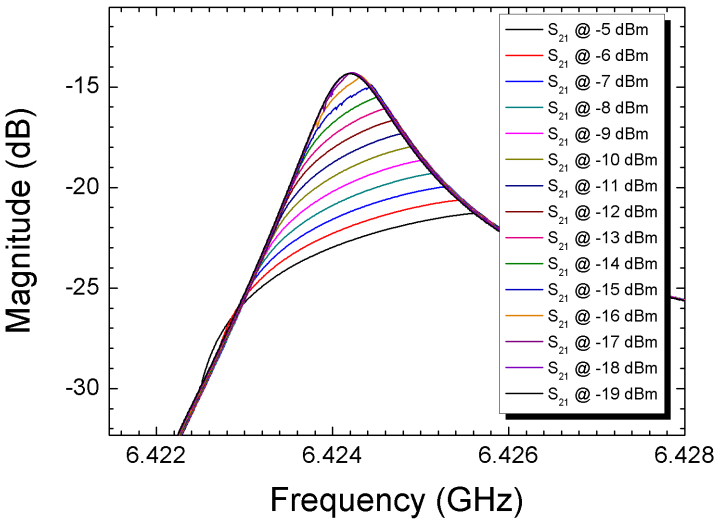

Figure 5.16: Transmission S_{21} of R21 on Silicon: Distortion of resonance peak with increasing input power.

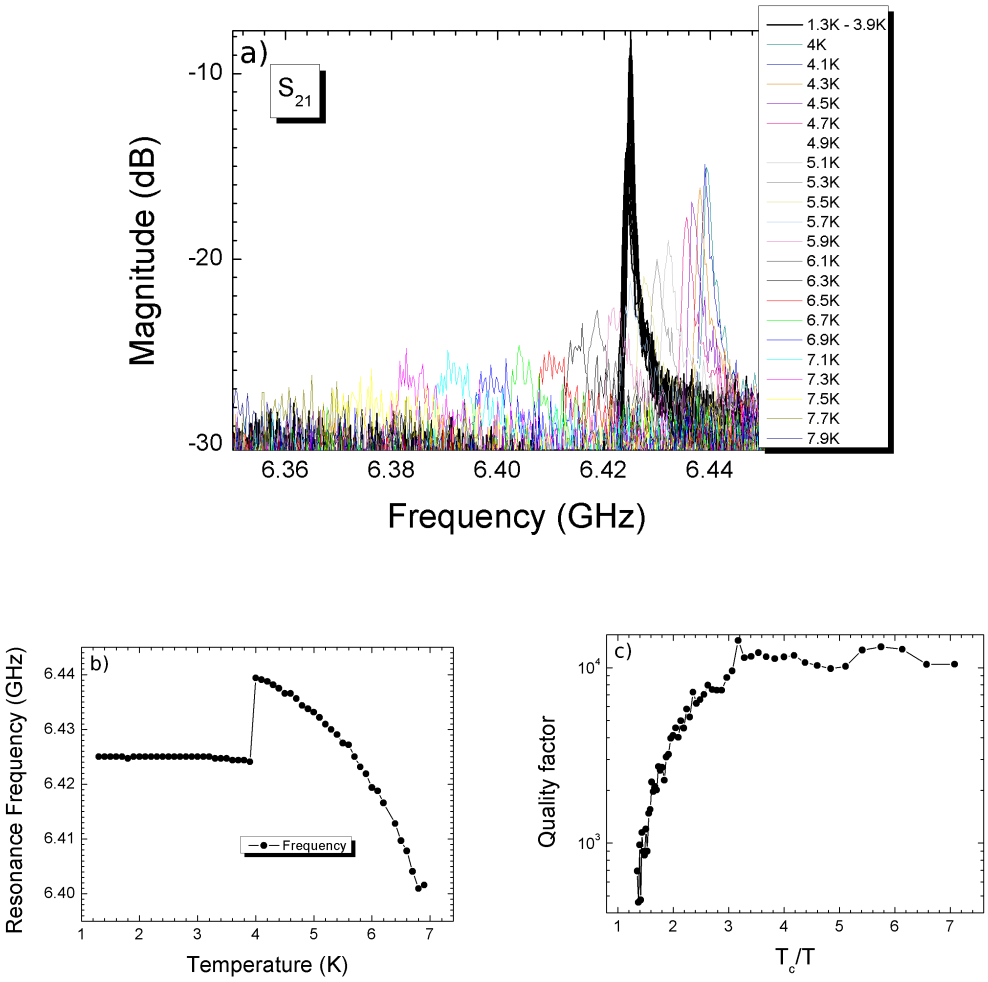

Figure 5.17: (a) Transmission S_{21} of R21 on Silicon at different temperatures, (b) dependence of the resonance frequency on temperature, (c) dependence of the quality factor on temperature.

5.3.2 R21 on Sapphire

name	design	W [μm]	S [μm]	length [mm]	frequency [GHz]	capacitance	value	substrate material
R21	Yale	5	10	9.759	6.4171	overcoupled	6.2 fF	Sapphire

Table 5.9: Description of the resonator R21 on Sapphire.

R21 on Sapphire leads to a shift of the resonance frequency of 0.11 GHz compared to R21 on Silicon (see Figure 5.18). Again the quality is lower on Sapphire than on Silicon.

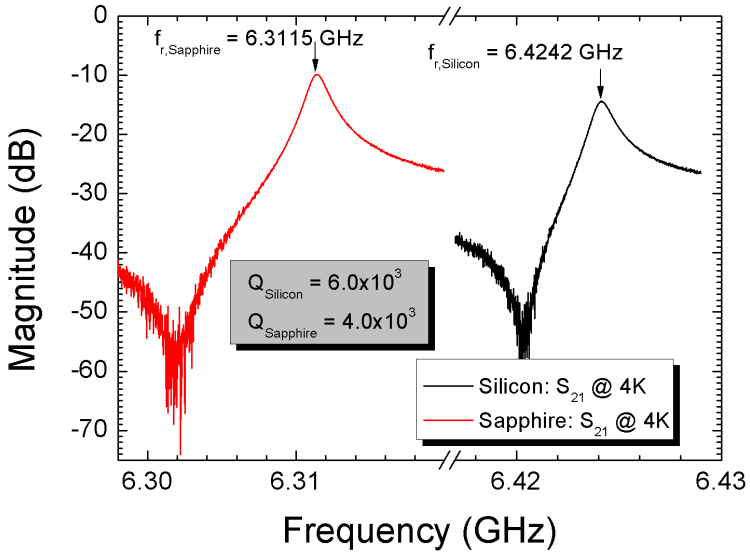

Figure 5.18: Comparison of transmission S_{21} of R21 on Silicon and Sapphire.

It is worth mentioning that no power distortion effect resulting definitely from the resonator was observed on any Sapphire sample. Although there are power distortion effects visible at values larger than -5 dBm, these discontinuities can also be referred to the NVA which is not calibrated above -5 dBm.

5.4 Measurement – Design 2: R36 on Silicon

name	design	W [μm]	S [μm]	length [mm]	frequency [GHz]	capacitance	value	substrate material
R36	design 2	20	50	9.854	6.38	overcoupled	31 fF	Silicon

Table 5.10: Description of the resonator R36 on Silicon.

The dimensions of the design 2 used for R36 are larger than in the two other designs. The capacitor is designed to be in between the overcoupled and undercoupled cases. In Figure 5.19 the transmission near the resonance at 4.5 and 1.5 K is shown. The quality factors are around 300. One could assume the value of coupling capacitance to be too high for better quality factors. The shift in resonance frequency can again be attributed to the change in the dielectric constant, caused by liquid Helium entering the box.

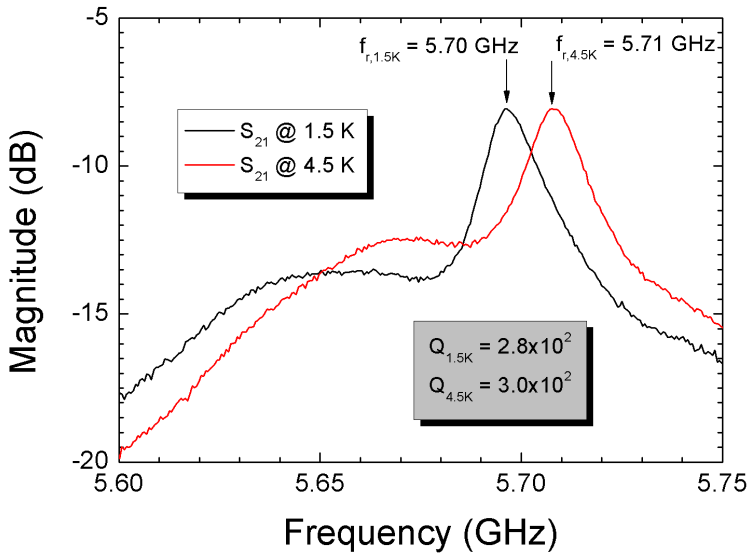

Figure 5.19: Transmission S_{21} of R36 on Silicon at 4 K and 1.5 K.

Figure 5.20 shows the transmission and reflection of R36 near the resonance. The qualities in reflection and transmission are of the same order of magnitude.

From comparison with the other designs (see Figure 5.5 and Figure 5.14) one could suggest that the higher the coupling, the higher the quality factor of reflection compared to the quality factor of transmission. The phase change at 5.69 GHz in Figure 5.7a verifies the resonance at this frequency.

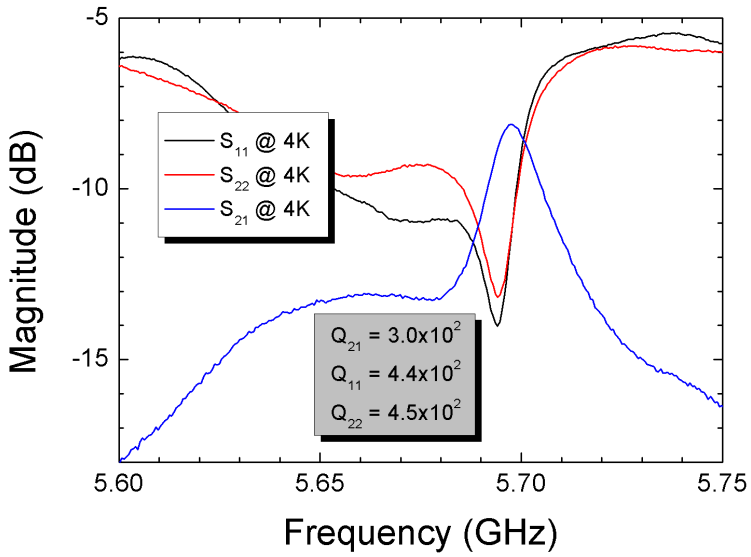

Figure 5.20: Transmission S_{21} and reflection S_{22} and S_{11} of R36 on Silicon at 4 K.

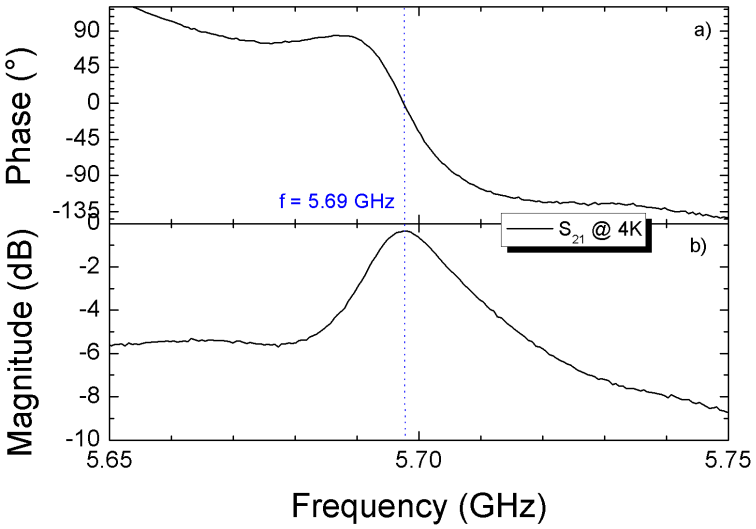

Figure 5.21: Transmission S_{21} of R36 on Silicon at 4 K with full calibrated cables: Phase shift (a) and magnitude (b) at resonance.

5.5 Discussion of the Experimental Results

This subsection analyzes the results and compares the resonance frequency and quality factors from theoretical predictions with measured values.

Figure 5.22 shows the influence of the coupling to the environment on the resonance frequency. For all resonators, except R27 which is designed for a different frequency, the resonance frequency decreases with increasing coupling. In the Yale design, in contrast to design 1, the resonance frequency is lower for Sapphire. This behavior is not predicted by theory.

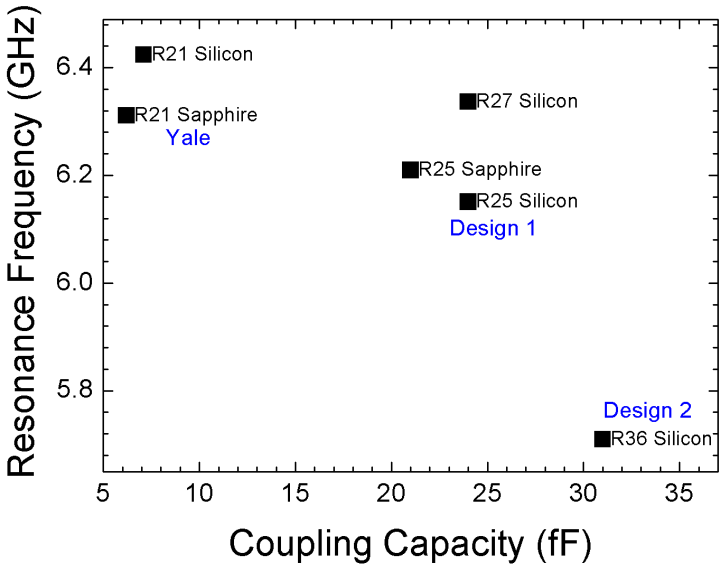

Figure 5.22: Measured resonance frequency versus coupling capacitance of all designs.

Figure 5.23 shows the dependence of the quality factor on the coupling capacitance. The influence of the design on the quality factor is clearly visible. With larger dimensions of the gap W and inner strip S the quality factor decreases. The reason for this effect can be stronger coupling to the environment, as it is the case for the resonance frequency dependence in Figure 5.22. As the loaded quality factor should approximately be the same for all designs (see tables at the end of this section) another explanation for the decrease of the quality factor could be other losses e.g. radiation losses that have yet been neglected in the calculations.

The Tables 5.11 to 5.15 compare theoretical predicted quality factors and resonance frequencies with measured results. The uncoupled resonance frequencies are calculated using (2.31), the quality factors are derived by inserting the values from Table 2.5 in (2.32). Coupled values are derived from the formulas (2.29) for the loaded resonance frequency and (2.28) for the loaded quality factor.

A loss tangent of $7{\cdot}10^{-4}$ was assumed for Silicon in order to have quality factors com-

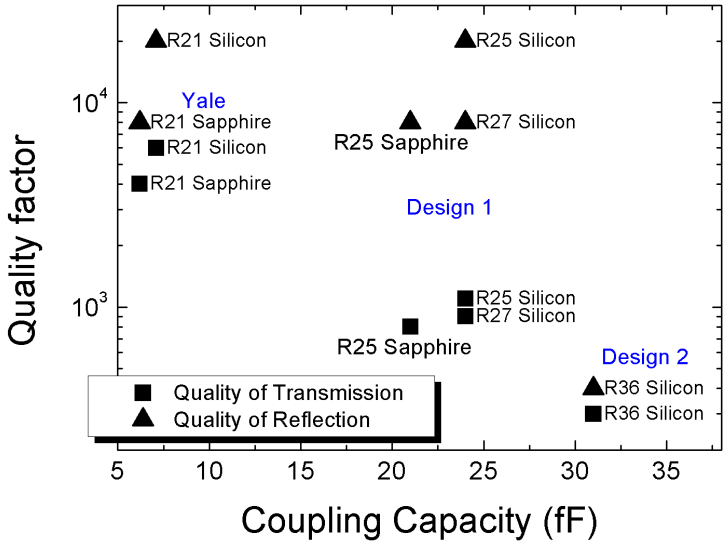

Figure 5.23: Measured quality factor versus coupling capacitance of all designs.

parable to the measurements. For R21 in Table 5.11 the results measured for Sapphire are comparable with theoretical prediction. Table 5.14 shows better measurement results than predicted for Silicon and worse results for Sapphire. Measurement and prediction for R27 are comparable for the quality factor as shown in Table 5.14, whereas in Table 5.15 the quality factors of prediction and measurement differ by two orders of magnitude.

In all measurements, except for R21 on Sapphire, the measured and the calculated resonance frequencies differ from ≈ 0.1 GHz to 0.6 GHz. We assume that parasitic reactances, not eliminated with our calibration scheme can influence the resonance frequency.

All calculations result in a higher quality factor for Sapphire than for Silicon, whereas measurements show the opposite result. Possibly, an improvement of the loss tangent of the Silicon substrates results from the fact that the Silicon Oxide layer on top of the Silicon was always etched away in the RIE process due to its small etching-resistivity. Therefore, the gap between the inner strip and the ground planes, where the electric and magnetic fields have their maximal values, is filled with Helium gas or liquid Helium which has a better loss tangent. The deviation of the quality factor in reflection of R25 and R27 could result from different etching depth on the Silicon Oxide layer.

Yale design designed for 5.85 GHz			uncoupled	**R20** undercoupled	**R21** overcoupled	
					calculated	measured
Silicon	coupling capacitance			(C_{uc} = 0.69 fF)	(C_{oc} =7.1 fF)	
	resonance frequency (GHz)	4 K	6.0168	6.0168	6.0166	6.4242
		50 mK	6.0176	6.0176	6.0174	6.4431
	quality factor	4 K	$3.6 \cdot 10^3$	$3.6 \cdot 10^3$	$3.6 \cdot 10^3$	$6.0 \cdot 10^3$
		50 mK	$1.6 \cdot 10^4$	$1.6 \cdot 10^4$	$1.5 \cdot 10^4$	$1.4 \cdot 10^4$
Sapphire	coupling capacitance			(C_{uc} = 0.58 fF)	(C_{oc} =6.2 fF)	
	resonance frequency (GHz)	4 K	6.4174	6.4174	6.4171	6.3115
		50 mK	6.4183	6.4182	6.4145	–
	quality factor	4 K	$4.5 \cdot 10^3$	$4.5 \cdot 10^3$	$4.4 \cdot 10^3$	$4.0 \cdot 10^3$
		50 mK	$6.9 \cdot 10^{10}$	$1.2 \cdot 10^8$	$1.0 \cdot 10^6$	–

Table 5.11: Calculated and measured resonance frequencies and quality factors for R20 and R21.

Yale design designed for 6.00 GHz			uncoupled	**R22** undercoupled	**R23** overcoupled
Silicon	coupling capacitance			(C_{uc} = 0.69 fF)	C_{oc} =7.1 fF)
	resonance frequency (GHz)	4 K	6.1711	6.1711	6.1708
		50 mK	6.1719	6.1719	6.1717
	quality factor	4 K	$3.6 \cdot 10^3$	$3.6 \cdot 10^3$	$3.6 \cdot 10^3$
		50 mK	$1.6 \cdot 10^4$	$1.6 \cdot 10^4$	$1.5 \cdot 10^4$
Sapphire	coupling capacitance			(C_{uc} = 0.58 fF)	(C_{oc} =6.2 fF)
	resonance frequency (GHz)	4 K	6.5820	6.5819	6.5817
		50 mK	6.5829	6.5828	6.5826
	quality factor	4 K	$4.3 \cdot 10^3$	$4.3 \cdot 10^3$	$4.3 \cdot 10^3$
		50 mK	$6.8 \cdot 10^{10}$	$1.1 \cdot 10^8$	$9.9 \cdot 10^5$

Table 5.12: Calculated resonance frequencies and quality factors for R22 and R23.

	design 1 designed for 5.85 GHz		uncoupled	**R24** undercoupled	**R25** overcoupled	
					calculated	measured
Silicon	coupling capacitance			(C_{uc} = 1.2 fF)	(C_{oc} =7.1 fF)	
	resonance frequency (GHz)	4 K	6.003	6.003	6.003	6.151
		50 mK	6.004	6.004	6.003	–
	quality factor	4 K	$5.6 \cdot 10^3$	$5.6 \cdot 10^3$	$5.2 \cdot 10^3$	$1.1 \cdot 10^4$
		50 mK	$1.6 \cdot 10^4$	$1.6 \cdot 10^4$	$1.3 \cdot 10^4$	–
Sapphire	coupling capacitance			(C_{uc} = 1.1 fF)	(C_{oc} =6.2 fF)	
	resonance frequency (GHz)	4 K	6.403	6.403	6.402	6.210
		50 mK	6.404	6.404	6.403	–
	quality factor	4 K	$8.2 \cdot 10^3$	$8.2 \cdot 10^3$	$7.5 \cdot 10^3$	$8 \cdot 10^2$
		50 mK	$8.3 \cdot 10^{10}$	$3.2 \cdot 10^7$	$8.9 \cdot 10^4$	–

Table 5.13: Calculated and measured resonance frequencies and quality factors for R24 and R25.

	design 1 designed for 6.00 GHz		uncoupled	**R26** undercoupled	**R27** overcoupled	
					calculated	measured
Silicon	coupling capacitance			(C_{uc} = 1.2 fF)	(C_{oc} =7.1 fF)	
	resonance frequency (GHz)	4 K	6.157	6.157	6.156	6.337
		50 mK	6.158	6.158	6.157	–
	quality factor	4 K	$5.5 \cdot 10^3$	$5.5 \cdot 10^3$	$5.1 \cdot 10^3$	$0.9 \cdot 10^3$
		50 mK	$1.6 \cdot 10^4$	$1.6 \cdot 10^4$	$1.3 \cdot 10^4$	–
Sapphire	coupling capacitance			(C_{uc} = 1.1 fF)	(C_{oc} =6.2 fF)	
	resonance frequency (GHz)	4 K	6.568	6.567	6.567	–
		50 mK	6.568	6.568	6.567	–
	quality factor	4 K	$8.0 \cdot 10^3$	$8.0 \cdot 10^3$	$7.3 \cdot 10^3$	–
		50 mK	$8.3 \cdot 10^{10}$	$3.2 \cdot 10^7$	$8.9 \cdot 10^4$	–

Table 5.14: Calculated and measured resonance frequencies and quality factors for R26 and R27.

	design 2 designed for 5.85 GHz		uncoupled	**R36** slightly overcoupled	
				calculated	measured
Sapphire	coupling capacitance			(C_{uc} = 31 fF)	
	resonance frequency (GHz)	4 K	6.39	6.38	5.71
		50 mK	6.39	6.38	–
	quality factor	4 K	$1.8 \cdot 10^4$	$1.2 \cdot 10^4$	$3.0 \cdot 10^2$
		50 mK	$9.6 \cdot 10^{10}$	$4.0 \cdot 10^4$	–

Table 5.15: Calculated and measured resonance frequencies and quality factors for R36 on Sapphire.

6 Simulations

This chapter gives a brief overview of the simulations done to predict the experimental results. For the simulations done at the Walther-Meißner-Institut the software Sonnet Lite was used. Additional calculations for the resonator R21 were done at the Institute of Nanoelectronics.

6.1 Simulations in Sonnet

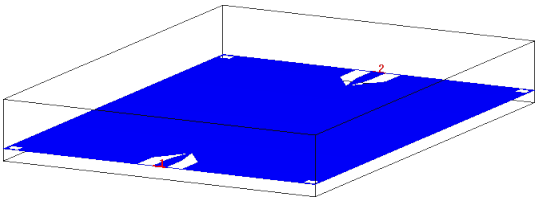

Figure 6.1: Structure in the gold plated box with two-ports as simulated in Sonnet

It is possible to include superconductivity in the simulations done with Sonnet by using the temperate and frequency dependent inductance derived in (2.26) on page 17. In the simulation process this inductance is multiplied with the frequency[1]. All simulations were performed for three different regimes, first Niobium as perfect conductor (labeled as nc), second at temperatures of 4 K and third at a temperature of 50 mK. The results in the superconducting regime do not vary much with temperature, therefore, both results are summarized in the superconducting (sc) results.

The following parameters were used in the simulations:

	4 K	50 mK
λ_L	47.9 nm	47 nm
L_s	0.060 pH	0.059 pH

Table 6.1: Inductance inserted in Sonnet to simulate superconductivity.

In the simulations we took advantage of the high symmetry of the resonator structure: A symmetry axis was laid in the middle of the center strip and Sonnet simulated only one half of the structure, extrapolating the second half. Thus the computer needed less memory and the necessary calculation time is reduced by a factor of 7. This procedure has been verified by comparing it to a simulation of the whole structure.

[1] See Sonnet manual page 70ff

6.1.1 Simulations of the Experimentally Realized Results

6.1.1.1 Yale

For the Yale design we were only able to simulate transmission lines (T20). The simulation program ran out of memory during the subsectioning of the resonators. Pictures of example meshes are shown in Figure 6.2. The analysis of the transmission lines gives a ground plane resonance at 5.46 GHz that occurs in all structures of the same geometry. The ground plane resonance depends weakly on the superconductivity of the structure.

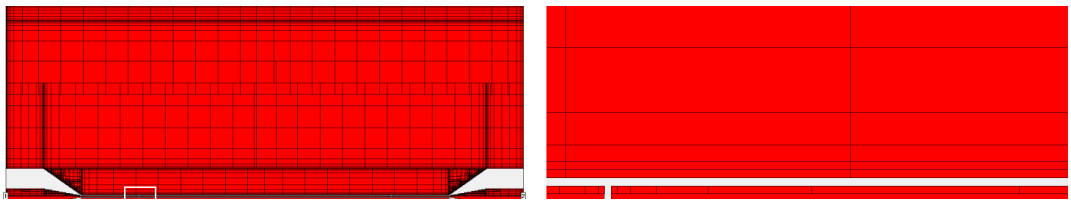

Figure 6.2: (a) Meshing done by Sonnet in the upper half of the resonator, due to the resolution of the picture no inner strip is visible in the lower range of the graph (b) enlargement of the white boxed region of (a), one can see the meshing near the inner strip and the gap.

6.1.1.2 Design 1

The simulations of design 1 revealed the results in Figure 6.3. With this design, simulations of resonators were possible. The ground plane resonance is distributed all over the structure of the transmission line T21.

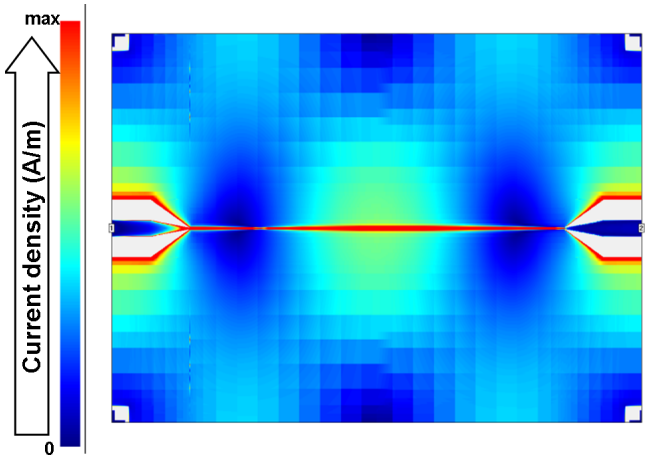

Figure 6.3: Simulation of the current distribution of T21 at the ground plane resonance frequency of 5.435 GHz.

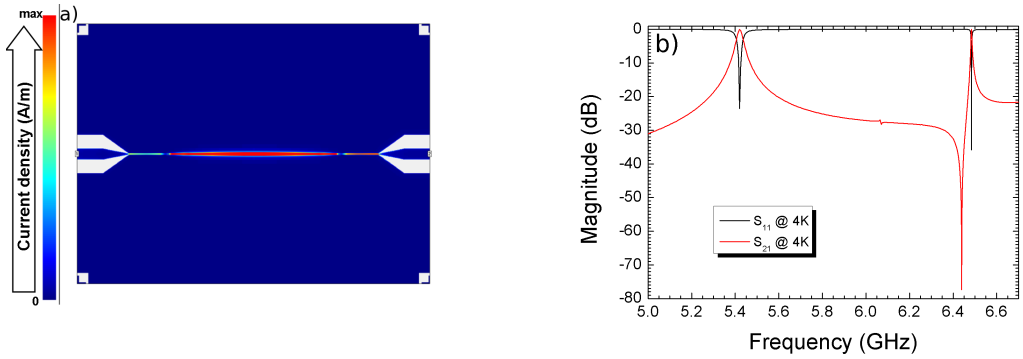

Figure 6.4: Simulation of the resonator R24 (a) Current distribution at the resonance at 6.485 GHz, (b) Backward transmission S_{12} and reflection S_{11}.

In this design the undercoupled resonators are analyzed with a meshing resolution sufficient to resolve the structures of the coupling capacitances. Figure 6.4(a) shows the current distribution of the resonator R24 at its resonance frequency. In Figure 6.4(b) one can easily identify the ground plane resonance at 5.42 GHz and the resonance frequency of 6.485 GHz. A summary of all measured resonators of design 1 is given in Table 6.2. R24 and R25 are designed for 5.85 GHz, R26 and R27 for 6.00 GHz. Even numbers are undercoupled, odd numbers are overcoupled. The software was not able to simulate the overcoupled resonators containing thin fingers, because of memory problems.

resonator	nc resonance (GHz)	sc resonance (GHz)
R24	6.54	6.485
R25	short	
R26	6.675	6.615
R27	short	

Table 6.2: Simulation results of design 1.

6.1.1.3 Design 2

The fabricated and measured resonator R36 has a medium coupling and was designed using design 2. Besides this resonator four other resonators with design 2, shown in Table 6.3, were simulated. These resonators have linear scaled coupling capacitors compared to the Yale design and design 1 (see also section 3.2).

R28 and R30 are undercoupled, R29 and R31 are overcoupled resonators with 6 fingers (instead of 2 and 3 at Yale and design 1, respectively). All structures have a ground plane mode at 5.4 GHz.

resonator	nc resonance (GHz)	sc resonance (GHz)
R28	6.41	6.388
R29	5.725	5.685
R30	6.62	5.59
R31	6.685	6.625
R36	6.065	6.035

Table 6.3: Simulation results of design 2.

6.1.2 Additional Designs

All resonators discussed in this subsection were designed for a resonance frequency of 5.85 GHz

6.1.2.1 Anritsu glass bead connectors for Sapphire and Silicon

In the Diploma Thesis of Andreas Emmert [5] the glas bead-connector from Anritsu is used. For using this connector a new flat pin of diameter 240 μm was designed. The designs using the Anritsu selfmade pin have their ground plane resonance at 5.6 GHz for Sapphire and at 5.2 GHz for Silicon, respectively, an even resonator number denotes undercoupling, while an odd number denotes overcoupling, label numbers smaller than 100 indicate Sapphire as substrate material, numbers greater than 100 indicate Silicon as substrate material. The Tables 6.4 and 6.5 show results for design 3 (W = 30 μm, S = 60 μm) and design 4 (W = 60 μm, S = 125 μm).

design 3

resonator	length D [μm]	nc resonance (GHz)	sc resonance (GHz)
R0	9864	6.375	6.35
R1		5.5	5.585
R100	9099	6.575	6.545
R101		5.92	5.875

Table 6.4: Simulation results of design 3 for the Anritsu glas bead connector.

design 4

resonator	length D [μm]	nc resonance (GHz)	sc resonance (GHz)
R2	9908	6.3	6.285
R3		short	
R102	9146	6.46	6.445
R103		short	

Table 6.5: Simulations results of design 4 for the Anritsu glas bead connector.

Figure 6.5 shows the colored ground plane mode of the transmission line T1 for the design 4.

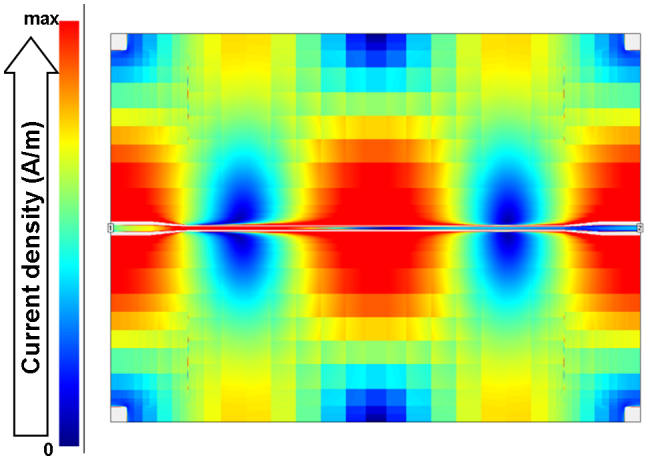

Figure 6.5: Current distribution for T1 at the ground plane resonance frequency of 5.56 GHz.

6.1.2.2 Rosenberger connector for Silicon

Also for the Rosenberger connector, resonators on Silicon following the designs 3 and 4 were simulated. The ground plane mode is at 5.1 GHz for both designs. In Table 6.6 again even resonator numbers denote undercouling, odd overcoupling.

resonator	design	length D [μm]	nc resonance (GHz)	sc resonance (GHz)
R120	design 3	9099	6.575	6.545
R121			5.91	5.845
R122	design 4	9146	6.46	6.445
R123			short	

Table 6.6: Simulation results of design 3 and 4 for the Rosenberger connector.

6.2 Simulations Done at the Institute of Nanoelectronics

Simulations on R21 were achieved by the Institute of Nanoelectronics of the Technical University of Munich in a collaboration within SFB 631. Here, the simulation of R21 on Sapphire, simulated with HFSS[2], is presented. This group also simulated resonators with loops in a gap, further information on this issue can be found in [4]. This structures were calculated assuming perfect conductors.

The group was able to simulate the R21 with a very sharp peak at 6.3170 GHz with a quality factor of about $1{\cdot}10^5$ in transmission. In Figure 6.6 the result of a simulation including forward and backward transmission and reflection is shown. Figure 6.7 shows the optimization process with a higher density of probe frequencies, but consuming more computing power. Also the method of numerical sweeps was changed to a more accurate way which resulted in a change of resonance frequency.

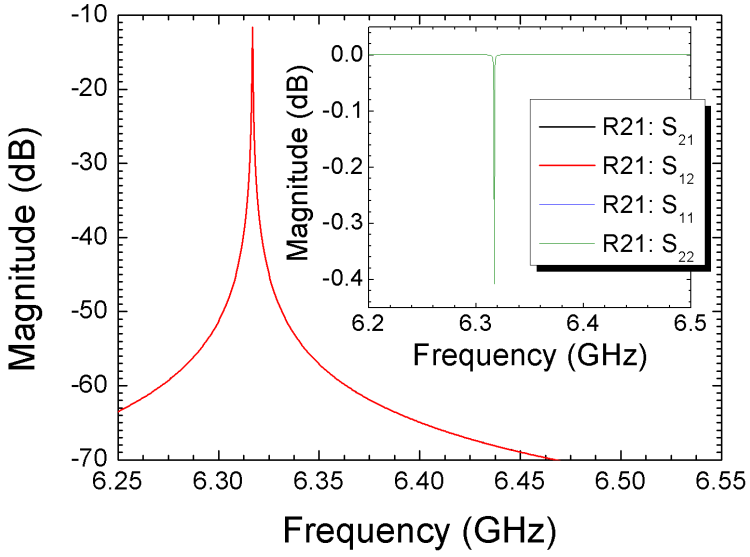

Figure 6.6: Forward and backward transmission S_{21} and S_{12} and forward and backward reflection S_{11} and S_{22} of R21 simulated at the Institute of Nanoelectronics.

In Figure 6.8 one can see a good agreement of simulation and measurement, with a deviation of 0.1 GHz. The quality factor of the measurement is 6000, the simulation gives $1{\cdot}10^5$.

[2] www.ansoft.com/products/hf/hfss/

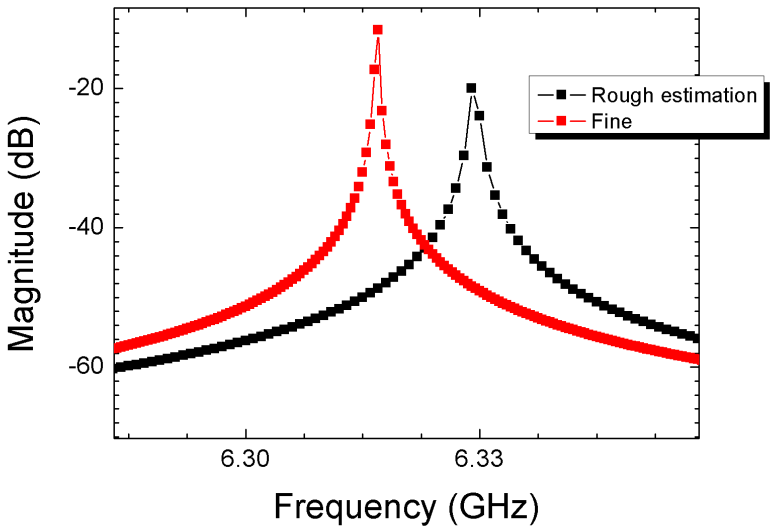

Figure 6.7: Simulated transmission S_{21} of R21 with increasing density of probe frequencies.

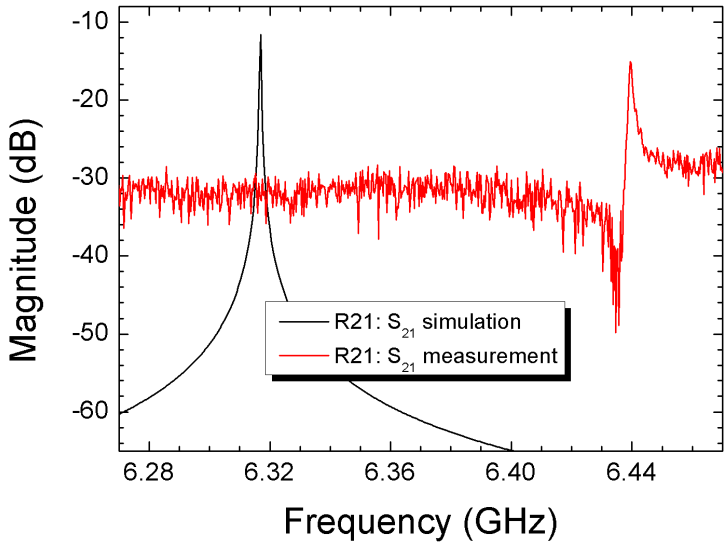

Figure 6.8: Comparison between measurement and simulation of the transmission S_{21} of R21 on Silicon.

7 Conclusion and Outlook

Three central issues on the way to quantum computing are a scheme for the readout of qubits, sufficiently long coherence times and coupling of qubits. A promising scheme has been realized in quantum optics where qubits couple strongly to cavities. Also, in solid state physics this scheme was realized by Wallraff et al. [21]. Among the realizations of solid state qubits, which are very interesting because of their potential scalability, superconducting qubits are of high interest because of their superconduction energy gap. Different realizations (charge qubits: the Cooper pair box, flux qubits) have an energy gap in the GHz regime. At the Walther-Meißner-Institut circuit QED experiments are planed with flux qubits which require appropriate resonators in the GHz regime, as realized in this thesis, in order to obtain the regime of strong coupling.

In this work, basic principles of coplanar waveguides were presented, the transmission line method favored for this thesis. Two different types of coplanar waveguides were discussed in detail, namely the conventional and the conductor backed coplanar waveguide. In a brief section we showed that the Silicon Oxide layer on the Silicon substrates should not influence the CPW characteristics. In the course of the treatment of the CPW, we showed that in the measurement range no dispersion disturbs the measurement. In order to evaluate the quality factor of the resonators, the relevance of attenuation was presented theoretically and we showed that the conductor loss gives the largest amount to attenuation, followed by the dielectric losses in the substrate. The loss tangent of Silicon at liquid Helium temperature was resolved in order to match the measured quality factors.

After this, the calculations for the CPW were extended for superconductivity. We presented the model of the kinetic inductance and extended the conductor losses with superconductivity. Finally, a term for the surface impedance of a superconductor was derived which was included in the Sonnet simulations.

The theoretical part went on with the theory of the resonator and presented the resonance frequency and the quality factor, two quantities of significance in this thesis. The effect of coupling the resonators to the environment on these quantities was discussed. At last, the difference between lumped element resonators and distributed resonator was discussed and the influence of superconductivity, especially the temperature dependence of the relevant parameters in the superconducting regime was introduced. A short section was devoted to the scattering-matrix, the measured quantity in this work.

We designed and fabricated three layouts of CPW resonators with different inner strip and gap width, denoted as Yale design, design 1 and 2. For each design an undercoupled and an overcoupled resonator were made. For fabrication Niobium was sputtered on Sapphire and Silicon substrates, the structure was created with a RIE process. After this the resonators were silver glued in a box and mounted in the cryostat.

We measured resonators with quality factor up to $1.5 \cdot 10^4$ at 1.3 K. The resonator R21, with the highest quality, in Yale design on Silicon, was also measured down to 17 mK where not further increase in the quality could be observed. For comparison further resonators were fabricated and tested: A resonator with the same geometry, but on a Sapphire substrate showed a quality factor in the same range as for Silicon. Strangely, the resonance frequency was shifted in the other direction than predicted by theory. Design 1 was tested with three resonators. Two resonators with the same substrate material (Silicon) but different length showed a shift in resonance frequency like theoretically expected and had the same quality factor. A comparison between the two substrate materials Silicon and Sapphire showed a quality factor for Silicon one order of magnitude larger than the quality factor of Sapphire. Theoretically, these quality factors should be equal. Finally, a resonator in design 2 with very large coupling capacitances was measured in order to see how these influence the resonance frequency and quality factor. Both showed a drastic decrease. The decrease in the resonance frequency was also predicted by theory, while the quality factor should be larger by two orders of magnitude. All resonances were analyzed for higher modes and investigating the frequency dependance of the phase. The resonators showed a temperature dependence of resonance frequency and quality factor predicted by theory. Also the power distortion described by Frunzio [6] was verified for Silicon substrates.

A number of simulations of resonators were made. At the Walther-Meißner-Institut Sonnet was used, which is able to simulate a superconducting resonator with a frequency dependent inductance. The best resonator measured in this thesis was simulated at the Institute of Nanoelectronics.

Since the measured resonators have quality factors sufficient for the needs of further experiment, the next steps should be an optimization of the coupling capacitors and the length of the resonator in order to tune the quality factor and the resonance frequency to the desired values. Therefore, it will be useful to design a mask with a transmission line, where the capacitances can be written by electron beam lithography, which will also be used for the definition of qubits in the cavity. This method is faster because the layout just has to be transferred from the computer to the E-beam machine and the time and costs for the production of a mask will be avoided. Also, larger values for center strip and gap should be fabricated in order to place a qubit with a larger loop area and therefore mutual inductance (which is responsible for the coupling of qubit to the resonator) inside the gap. In order to have better calibrated measurements which would give a higher accuracy, measurements should be done in the probing station. Therefore, new probing tips are available with are suitable for cryogenic experiments. Preliminary recent experiments on R41 covered by gold have been done in the probing station, giving promising results. Of course the quality factor was quite low because of damping in the gold layer.

A Specimen Overview

Designs for Rosenberger Connectors with Sapphire as substrate material (see section 3.3)

labeling	design	designed for	capacitors	on mask
R20	Yale	5.85 GHz	undercoupled	1/2
R21	Yale	5.85 GHz	overcoupled	1
R22	Yale	6.00 GHz	undercoupled	1
R23	Yale	6.00 GHz	overcoupled	1
R24	design 1	5.85 GHz	undercoupled	1
R25	design 1	5.85 GHz	overcoupled	1
R26	design 1	6.00 GHz	undercoupled	1
R27	design 1	6.00 GHz	overcoupled	1
R28	design 2	5.85 GHz	undercoupled	1
R29	design 2	5.85 GHz	overcoupled	
R30	design 2	6.00 GHz	undercoupled	1
R31	design 2	6.00 GHz	overcoupled	1
R36	design 2	5.85 GHz	slightly overcoupled	1

All resonators in the table above have also been designed for the probing station (on mask 2). These designs are labeled with numbers increased by 20.

B Masks

B.1 Mask for Rosenberger Connector

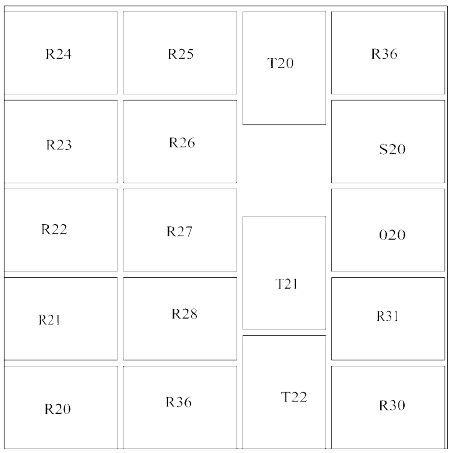

B.2 Mask for Probing Station

Bibliography

[1] *INFORMATIK: Quantenchip aus Kanada*, DER SPIEGEL **8** (2007).

[2] A. Blais, R.-S. Huang, A. Wallraff, S.M. Girvin, and R. J. Schoelkopf, *Cavity quantum electrodynamics for superconducting electrical circuits: an architecture for quantum computation*, Phys. Rev. A **69** (2004), 062320.

[3] R. E. Collin, *Foundations for Microwave Engineering, Second Edition*, Wiley-IEEE Press, (New Jersey), 2000.

[4] G. Csaba, Z. Fahem, F. Peretti, and P. Lugli, *Circuit modeling of flux qubits interacting with superconducting waveguides*, Journal of Computational Electronics (2007).

[5] A. Emmert, *Circuit-quantum electrodynamics (CQED) with superconducting flux qubits*, Diploma thesis, Technische Universität München, 2006.

[6] L. Frunzio, A. Wallraff, D. Schuster, J. Majer, and R. Schoelkopf, *Fabrication and characterization of superconducting circuit qed devices for quantum computation*, IEEE Trans. Appl. Supercond. **15** (2005), 860.

[7] Kessler Jochen, *Untersuchung hochtemperatursupraleitender planarer wellenleiter mittels partialwellensynthese*, Ph.D. thesis, Technische Universität München, 1992.

[8] H. Keesom, *Helium*, Elsevier, 1942.

[9] Jerzy Krupka, *Dielectric measurements on low-loss materials*, Instytut Mikroelektroniki i Optoelektroniki PW (Warszawa, Poland) (2002).

[10] M. Mariantoni, *private communications*.

[11] M. Mariantoni, M.J. Storcz, F.K. Wilhelm, W.D. Oliver, A. Emmert, A. Marx, R. Gross, H. Christ, and E. Solano, *On-Chip Microwave Fock States and Quantum Homodyne Measurements*, cond-mat/0509737 (2006).

[12] Thomas Niemczyk, *Superconducting Microwave Circuits for Quantum Experiments*, Diploma thesis, Technische Universität München, 2006.

[13] D. M. Pozar, *Microwave Engineering, Third Edition*, John Wiley & Sons, Inc., (New York), 2005.

[14] S. Ramo, J.R. Whinnery, and T. v. Duzer, *Fields and waves in communication electronics*, John Wiley & Sons, Inc., (New York), 1994, 3rd ed.

[15] JP Reithmaier, G. Sek, A. Loeffler, C. Hofmann, S. Kuhn, S. Reitzenstein, LV Keldysh, VD Kulakovskii, TL Reinecke, and A. Forchel, *Strong coupling in a single quantum dot-semiconductor microcavity system*, Nature **432** (2004), no. 7014, 197–200.

[16] Peter Russer, *Electromagnetics, microwave circuit and antenna design for communications engineering*, Artech House Antennas and Propagation Library, vol. 2, Artech House, March 2006.

[17] P. Shor, *Algorithms for quantum computation: Discrete logarithms and factoring*, in Proc. 35th Ann. Symp. on the Foundations of Computer Science (ed. S. Goldwasser), IEEE Computer Society Press, Los Alamitos, California **1** (1994), 124–134.

[18] R. N. Simons, *Coplanar Waveguide Circuits, Components, and Systems*, John Wiley & Sons, (New York), 2001.

[19] Alejandro Arnoldo Valenzuela, *Hochfrequenzeigenschaften supraleitender $YBa_2Cu_3O_{7-\delta}$-Dünnschichten*, Ph.D. thesis, Technische Universität München, 1991.

[20] L.M.K. Vandersypen, M. Steffen, G. Breyta, C.S. Yannoni, M.H. Sherwood, and I.L. Chuang, *Experimental realization of shor's quantum factoring algorithm using nuclear magnetic resonance*, Nature **414** (2001), 883–887.

[21] A. Wallraff, D.I. Schuster, A. Blais, L. Frunzio, R.-S. Huang, J. Majer, S. Kumar, S.M. Girvin, and R.J. Schoelkopf, *Strong coupling of a single photon to a superconducting qubit using circuit quantum electrodynamics*, Nature **431** (2004), 162–167.

[22] Cheng P. Wen, *Coplanar Waveguide: A surface strip transmission line suitable for nonreciprocal gyromagnetic device applications*, IEEE **17** (1969), 1087–1090.

[23] C.-P. Yang, S.-I Chu, and S. Han, *Quantum information transfer and entanglement with squid qubits in cavity qed: A dark-state scheme with tolerance for nonuniform device parameter*, Phys. Rev. Lett. **92** (2004), 117902.

List of Figures

List of Tables

Danksagung

Vor allem möchte ich mich bei *Prof. Dr. Rudolf Gross* bedanken, dass er mir diese Arbeit, die mir sehr viel Freude bereitet hat, ermöglicht hat und mir mit Rat und Tat zur Seite gestanden hat.

Dr. Achim Marx danke ich, dass er immer für mich da war und mich unterstützt hat, wo immer ich Probleme hatte. Der ganzen *QUBIT-Gruppe* danke ich für die freundliche Aufnahme im besonderen *Matteo Mariantoni* für die Begeisterung für das Diplomarbeitthema, die Unterstützung beim Ausarbeiten der Theorie und das Design der Gold plated box. *Tomasz Niemczyk* danke ich herzlich für seine Hilfe bei Herstellung, Messaufbau, Messungen, Sputtern, Belichten..., einfach allem was wir miteinander gemacht haben. Tomasz, ohne Dich wäre die Diplomarbeit nie so erfolgreich geworden. *Georg Wild* danke ich für die ständige Bereitschaft mir wieder einen Carrier aus der Sputterkammerzuführung zu retten. Danke an *Edwin Menzel* der zum Glück immer genug Zeit hatte, wenn ich irgendwelche Probleme hatte (und zum Glück auch alles kann). Für die ständige Hilfsbereitschaft und die freundliche Aufnahme danke ich auch *Tobias Heimbeck*, *Karl Madek*, *Frank Deppe* und *Sonia Dandl*. *Elisabeth Hoffmann* wünsche ich eine ebenso erfolgreiche Diplomarbeit wie meine es war und bedanke mich bei ihr für das ständige Nerven ob sie noch etwas Korrekturlesen soll und Ihre Rücksicht während des Schreibens. Ich hoffe die angedrohten Kinobesuche und Kaffekränzchen mit ihr wahr machen zu können.

Aus meinem Büro danke ich noch *Sebastian Jakob* für das angenehme Arbeitsklima und das Korrigieren der Diplomarbeit.

Meinen Kommilitonen *Wolfgang Kaiser* und *Ludwig Klam* vielen Dank für die ständig offenen Ohren und die lustigen Gespräche. Dietrich Einzel danke, dass ich immer reinschneien konnte und für die makroskopische Wellenfunktion.

Robert Müller, *Helmut Thies*, *Thomas Brenninger*, *Joachim Geismann*, *Sigfried Wanninger*, *Dieter Guratsch*, *Gabriele Goerblich*, *Jutta Laaser*, *Emel Dönertas* und *Tina Pinkert* danke ich für Ihre Hilfe bei Problemen, dem *Reinigungsteam* für nette Gespräche.

Meinen *Eltern* danke, dass sie mir das Studium möglich gemacht haben und mich wo es ging unterstützt haben, ihnen und *meinen Geschwistern* für Gebete und für den Rückhalt während der Diplomarbeit.

Meinem Freund *Andreas*, der mich immer unterstützt hat und mir während meiner heißen Phase der Diplomarbeit die Probleme vom Hals gehalten hat, danke dafür.

Danke an alle meine *Freunde* für den Spass, die Unterstützung während des Studiums und die meet-and-eat-Abende, besonders *Claudia Fellner* für die leckeren Mittagessen.